DYNAMICS OF CRACKED STRUCTURES USING FINITE ELEMENTS

A THESIS

Presented to

The Faculty of the Division of Graduate

Studies and Research

By

Joseph David Morgan, III

In Partial Fulfillment

of the Requirements for the Degree

Doctor of Philosophy in the

School of Engineering Science and Mechanics

Georgia Institute of Technology

June, 1974

DYNAMICS OF CRACKED STRUCTURES USING FINITE ELEMENTS

Approved:

J. M. Anderson, Chairman

W. W. King

A. Aberson

R. L. Carlson

Date approved by Chairman: 5/17/1974

ACKNOWLEDGMENTS

The inspiration, encouragement, and guidance of Dr. J. M. Anderson, Dr. W. W. King, Dr. R. W. Shreeves and Dr. J. A. Aberson, of the School of Engineering Science and Mechanics, and of Dr. R. L. Carlson, School of Aerospace Engineering, made possible the completion of this work. Particular thanks are due to Dr. Anderson for his service as major professor and for my introduction to fracture mechanics, to Dr. King for his invaluable epistemological insights and to Dr. Aberson for his computer programming assistance. I am intellectually and philosophically indebted to Professor W. H. Horton and to Dr. M. B. Sledd. Each of these gentlemen contributed materially, as teacher and as friend, to this work.

The United States Air Force, via the Air Force Academy Instructor program of the Air Force Institute of Technology's Civilian Institutions Division, sponsored this work. A special thanks is due to Colonel P. J. Erdle, Vice Dean, United States Air Force Academy, for his assistance.

Finally, my wife Karen supplied unlimited patience and understanding during long periods of being essentially without a husband. But for her, this work would have been impossible.

TABLE OF CONTENTS

TABLE OF CONTENTS (Continued)

LIST OF TABLES

LIST OF ILLUSTRATIONS

SUMMARY

This work details the development, test and application of a dynamic finite element capability for analysis of cracked linearly elastic two-dimensional structures. The dynamic capability was obtained by determining the inertia properties (consistent mass matrices) for two previously developed and well tested high-order cracked elements. The mass matrices for an eight-node element which can represent only symmetric (Mode I) displacements and a ten-node element able to represent both antisymmetric (Mode II) and symmetric displacements were constructed by the generalized coordinate method. The coordinate functions were the Williams' series displacement eigenfunctions and rigid body displacement functions.

For computational economy, the cracked elements were homogeneous, constant thickness and fixed as to geometrical shape. Matrix dependence on material properties was made explicit by appropriate nondimensionalization and arrangement of the coordinate functions. The matrix elements, generated by numerical quadrature, were stored as DATA statements in FORTRAN subroutines. The mass matrix construction process is given in detail, including the nondimensionalization, schematic representations of all matrices and vectors, and numerical quadrature methods.

A UNIVAC 1108 FORTRAN V computer program with equilibrium, frequency eigenvalue, harmonic vibration and undamped transient dynamic response solution capability was written. The program library

includes the two cracked elements, the constant-strain triangle, a linear spring and a point mass. A program listing is not given.

The cracked element inertia properties were verified in two ways. First, the finite-element-model-predicted natural frequencies were compared with experimental frequencies for a square cracked plate. Model configurations and results are given. Predictions and experimental results agree very closely. Second, the time-dependent stress intensity factor for a finite crack opened by uniform pressure applied suddenly on the crack faces was computed and compared with a published analytic solution for an infinite plane. These results are presented in graphical form. The finite element values agree excellently with the analytic solution.

Simplified tup load-time data from an instrumented impact test of a pre-cracked Type A Charpy specimen were used to illustrate the effectiveness and efficiency of this finite element capability in a typical application. The variation of stress intensity factor with time obtained from the finite element model agrees well with recent analytic and analog computer results. This example clearly demonstrates the high-order element's ability to accurately represent wave propagation phenomena. Detailed load-time and specimen time-to-fracture records, "interpreted" by a finite element model, could provide a very economical means to determine material critical stress intensity factor (K_{IC}) values.

The finite element equations of motion for undamped linear elastodynamic systems, a complete derivation of the Williams' eigenfunction series solution for a cracked linearly elastic two-dimensional

continuum and a derivation of the particular version of the Newmark-β time integration operator used in the computer program are given in appendices.

CHAPTER I

INTRODUCTION

Fracture mechanics, long a challenging area for research in solid mechanics, is currently of considerable technological importance. Principally, this importance arises from the recent widespread use of high-strength, low-toughness materials in many structural applications, particularly in military and commercial aircraft.

For those configurations amenable to a two-dimensional treatment, the usual linear elastic fracture mechanics analysis of a given crack/structure/load system requires that the stress intensity factors K_I and K_{II} be determined. These factors are measures of the crack-tip stress-singularity strength for the opening and sliding crack face displacement modes shown in Figure 1. The stress intensity factors are defined in terms of the near-tip stress field in equations (A66) and (A67), Appendix A. Symbolic mathematical solutions for K_I and K_{II} are necessarily limited to simple configurations and boundary conditions, and extrapolation of such results to cracked structures of engineering interest is as much art as science.

To circumvent this limitation, the power of the finite element method [1-7]* was brought to bear. Early attempts to solve crack problems by finite element techniques [8-12], used only conventional elements. These elements did not incorporate the characteristic

*Numbers in square brackets correspond to reference on page 88.

crack-tip stress singularity [13] and models using them were necessarily very detailed near a crack tip. The stress and displacement fields in the near-tip region were ill represented, and stress intensity factors had to be extrapolated from values of the stresses or displacements at points away from the crack tip. Such refined models were costly and inefficient.

The situation for plane elastic analyses was much improved by the development of specific finite elements which incorporated the crack tip stress singularity. Such elements are called "singularity elements" or "cracked elements" and are based on the Williams' eigenfunctions [14-16] (Appendix A). Several early investigators created elements which incorporated only the singular eigenfunction [17-20], although one [21] used the first four symmetric eigenfunctions. Generally, these elements provided improved accuracy and were more economical to use.

Recently two "high-order" singularity elements were developed at the Georgia Institute of Technology and the Lockheed-Georgia Company [22]. The elements were called high-order elements because Williams' eigenfunctions of order higher than the first were incorporated. The eight-node element shown in Figure 2, can represent only symmetric (Mode I) deformations. It incorporates the first thirteen symmetric Williams' eigenfunctions. The ten-node element shown in Figure 3 can represent both symmetric and antisymmetric (Mode II) deformations. It incorporates the first nine symmetric and the first eight antisymmetric Williams' eigenfunctions. These high-order elements gave much more accurate results and were significantly more

economical than earlier elements.

With the success of the high-order singularity elements, the equilibrium analysis of plane elastic through-cracked structures by the finite element method was well in hand. The corresponding dynamic analysis seems to have been wholly neglected. This neglect is understandable, for although finite element dynamic solutions are well known [1-4], the computation times for such solutions are frequently orders of magnitude greater than those for the corresponding equilibrium problem. Thus, in the absence of an effective singularity element, dynamic finite element analysis of cracked structures is prohibitively expensive.

Motivated by the successful application of high-order elements to the solution of equilibrium problems, this research was undertaken to establish a dynamic finite element analysis capability for linearly elastic plane structures. To do so, it was necessary to determine the inertia properties (consistent mass matrices) for the high order elements, to incorporate these mass matrices (and the corresponding stiffness matrices [23,24]) into a computer program, and to verify element performance by application of the program to suitable test problems. This research advances the art of application of finite element methods to the dynamics of elastic fracture mechanics, providing a rational analysis capability for problems heretofore intractable. The major contribution is construction and verification of the mass matrices, since other aspects of the work are largely applications of existing concepts.

Since the high-order elements incorporate a stress singularity

and do not satisfy interelement displacement compatibility conditions [1,3,25], some investigation of the finite element solution convergence properties was required.

The finite element method has been rigorously established as a generally applicable mathematical technique for approximate solution of a very wide class of problems [1,3,4,25]. Convergence to the exact solution has been shown to occur, under very broad restrictions, as element size is reduced. For plane elasticity problems convergence is monotonic if the finite elements used to represent the continuum are compatible. For plane elasticity extensional solutions, elements are compatible if displacements along interelement boundaries are everywhere continuous. If the elements are not compatible, convergence can still occur, but is not necessarily monotonic. In some cases incompatible elements actually speed up the convergence [1,3]. Although the convergence proof in [25] assumes a nonsingular stress field, recent work by Tong and Pian [26] shows that convergence is still obtained when the finite element method is applied to a problem where the stress field is singular. Convergence in this case is largely controlled by the nature of the singularity. The opinion of Tong and Pian that the crack tip singularity should be taken into consideration by including the singular terms in a finite region, not too small in comparison with the crack length, is supported by the results of this and of earlier investigations [22].

The mass matrices developed in this work are called "consistent" mass matrices. A consistent mass matrix is one which is constructed using the same coordinate functions used for the stiffness matrix [27].

Equations (B12) and (B13) of Appendix B show explicitly the relationship involved.

While the consistent mass matrix is certainly a correct formulation, it is not the only choice [4,28]. There is considerable computational advantage in using a diagonal or "lumped" mass matrix [29] as well as some reduction [30] of the displacement oscillations preceeding wave front arrival, usually seen in consistent mass matrix model results. The question of an optimal diagonalization method is still open [29]. For the 10-node element, lumping the mass so as to preserve translational kinetic energy resulted in negative mass matrix elements corresponding to the y-displacement at two nodes. The "eigenfrequency preserving" technique of [29], although undoubtedly worthy of further study, was not pursued in this investigation.

The general small displacement equations of motion for a linearly elastic finite element are developed in Appendix B. The equations are then specialized to the particular elements developed in this research. The method for direct assembly of the element matrices into the structural matrices, which is not peculiar to this investigation, is not discussed.

Appendix A presents a detailed development of the Williams' eigenfunction series used as coordinate functions in construction of the singularity elements. This series was originally found by M. L. Williams [14], using the general stress function formulation for plane elasticity as developed by Love [31] and given in plane polar coordinates by Coker and Filon [32]. The derivation in the Appendix uses the stress function form given by Timoshenko and Goodier [33] and

an economical method of procedure used in [34]. The complete development was carried through in order to fully investigate the eigenvalue problem and because more displacement eigenfunctions were needed than were given by Williams. The stress and displacement series, taking account of the modified notation, agree with Williams' results [14] as corrected in [16]).

In Chapter 2, the displacement eigenfunctions of Appendix A and the finite element equations of Appendix B are used to construct the mass matrices. The equations implemented, the numerical techniques used and the checks made at each stage of the construction are described in detail. Tables show the structure of the necessary vectors and matrices. As part of the verification process the natural frequencies predicted by a finite element model for harmonically excited square cracked plates were compared with experimental values. This experimental work was carried out by Mr. John Malluck, a graduate student at the Georgia Institute of Technology [35].

Appendix C gives the detailed development of the time integration algorithm used in the transient dynamic analysis subroutine. The method is a version of the Newmark-β algorithm [36,37] as developed in difference equation form by Chan, Cox and Benfield [38].

Chapter 3 presents a brief description of the computer program developed to use the singularity elements and the finite element solutions to two problems. The first problem is a finite length through crack in an initially quiet infinite medium, with the crack faces loaded by a Heaviside step function normal pressure. This problem was chosen because a solution has been published [39,40], and

because it provided a severe test of element performance. The second problem, a Charpy impact test [41], was selected as an example of a useful dynamic application of the cracked element. The results are in good agreement with recently published reports [41,42].

Finally, Chapter 4 summarizes the main results of this investigation, points out some appropriate extensions of the work, and makes recommendations for further study in this area.

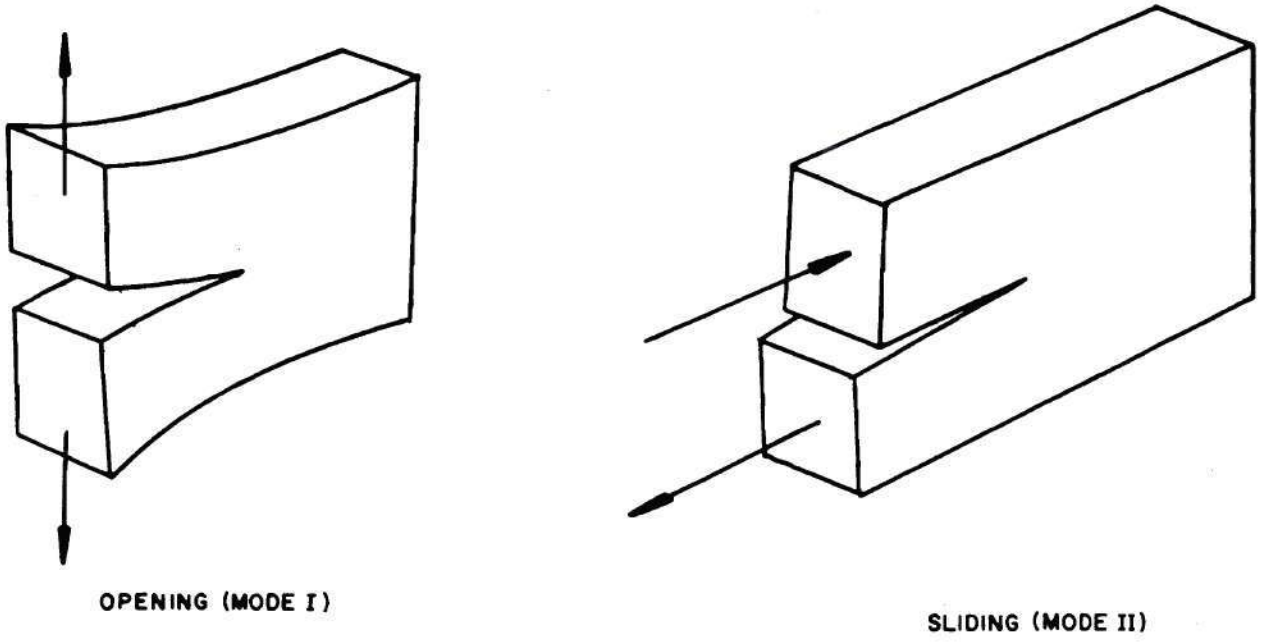

Figure 1. Crack Face Displacement Modes.

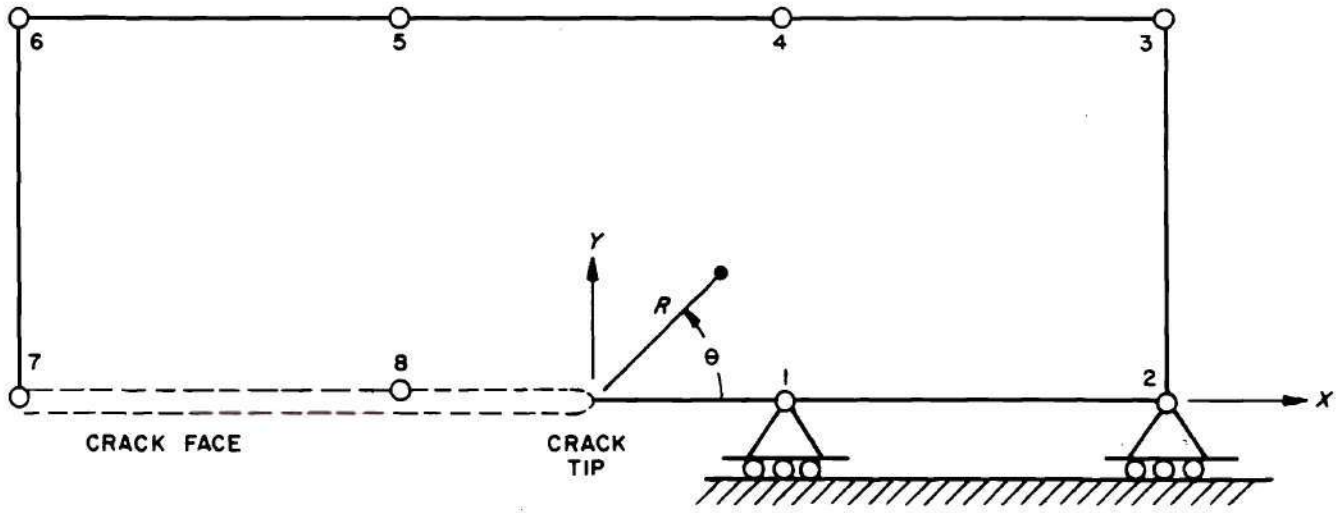

Figure 2. The Eight-Node Element.

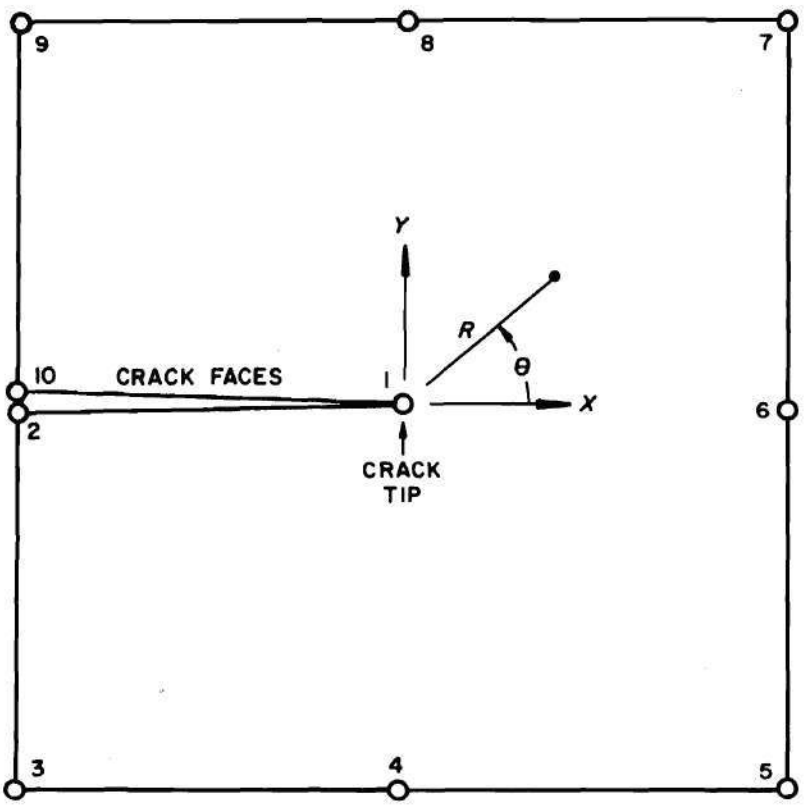

Figure 3. The Ten-Node Element.

CHAPTER II

CONSTRUCTION OF THE MASS MATRICES

This chapter shows the construction of the consistent mass matrices for the eight-node (Figure 2) and the ten-node (Figure 3) high-order singularity elements. The notation used is that of Appendices A and B.

Preliminary Considerations

Element Shape and the Coordinate Functions

Construction of the consistent mass matrices requires evaluation of equations (B17). These equations, in turn, depend on the structure of the $\underset{\sim}{f}$ matrix and on element shape.

The $\underset{\sim}{f}$ matrix consists of selected Williams' displacement eigenfunctions and rigid body terms. Its form is largely arbitrary. In this investigation, the $\underset{\sim}{f}$ matrices agree with those of [23,24], as do the element shapes. The $\underset{\sim}{f}$ matrix arrangement for the eight-node element is schematically depicted in Table 1, and the ten-node element $\underset{\sim}{f}$ matrix is shown in Table 6. Notation in both tables is that of equations (A61b) and (A62b) of Appendix A.

Element shape is chiefly limited by the requirement that the $\underset{\sim}{A}$ matrix be nonsingular. The $\underset{\sim}{A}$ matrix for each of the elements is well conditioned with respect to inversion, a single-precision inversion and check multiplication giving maximum off-diagonal terms of order 10^{-6}.

Computational Strategy and the Computer Program

In many finite element applications, the magnitude of the computational task is a major concern. Both large structures and sophisticated elements tend to increase the amount of computation required. In most finite element programs, the element matrices are integrated anew each time a problem is run. If this were done with the cracked elements each use would require duplication of the stiffness matrix and mass matrix integrations. The experience of earlier investigators was that such integration-at-each-use was economically unsound, considering the relative computer run times involved in performing the integration and in solving a typical problem after the matrices were generated [23,24]. This finding was confirmed. Attainment of adequately accurate mass matrix coefficients required UNIVAC 1108 run times of about five minutes, while problem solution run times for the problems in Chapter III were approximately three minutes.

The strategy adopted was to compute accurate values of required matrix elements in a nondimensional form for an element of constant thickness t, homogeneous mass density ρ and fixed shape. These coefficients were then stored as DATA statements in FORTRAN subroutines of the structural computer program.

When nondimensionalized equation (B17a) becomes

$$\underset{\sim}{M}_c = \rho t L^2 [\underset{\sim}{M}_{c11} + s\underset{\sim}{M}_{c12} + s^2 \underset{\sim}{M}_{c22}] \quad , \tag{2.1}$$

where

$$\underset{\sim}{M}_{c11} = \int_{\bar{A}} \underset{\sim}{f}_1^T \underset{\sim}{f}_1 d\bar{A} \quad , \tag{2.2a}$$

$$\underset{\sim}{M}_{c12} = \int_{\bar{A}} (\underset{\sim}{f}_1^T \underset{\sim}{f}_2 + \underset{\sim}{f}_{2n1}^T) d\bar{A} \tag{2.2b}$$

and

$$\underset{\sim}{M}_{c22} = \int_{\bar{A}} \underset{\sim}{f}_2^T \underset{\sim}{f}_2 d\bar{A} \ . \tag{2.2c}$$

$\bar{A}$ is the (nondimensionalized) element area, and L is a characteristic length, which in the program is element nodal point spacing.

In addition to the $\underset{\sim}{M}_c$ matrices, the $\underset{\sim}{K}_c$ and the $\underset{\sim}{A}$ matrices were stored in DATA statements.

Integration

Basic Considerations

Equations (2.2) can be evaluated as iterated integrals for each matrix component. Such families of integrals are sometimes reducible to combinations of a few standard types. For the eight-node and the ten-node elements the element boundaries are easily expressible in plane polar coordinates, but lead to unwieldy integrands for the second integration. Aside from the formidable amount of labor and certainty of algebraic error in reducing the hundreds of integrals involved, this approach offers no flexibility in the event a change in element shape is required. For these reasons and for ease of programming, numerical quadrature was used to calculate the mass matrix coefficients.

The integrands in equations (2.2) are all continuous over the region of integration and therefore may be treated by many numerical integration rules [44]. A factor which required careful consideration

was the oscillatory nature of the integrands. Such oscillatory integrands are most effectively handled by Filon quadrature [45-47]. Unfortunately Filon quadrature could not be used since it requires an explicit expression for each integrand. The matrix elements corresponding to the most rapidly oscillatory integrands were closely monitored throughout the mass matrix development. For a small number of integration points these elements did display the erratic behavior mentioned in [44] but became well behaved as the number of integration points was increased. These oscillatory integrands were not a controlling factor in this investigation. They might be more troublesome in construction of a more complex higher-order element involving Williams' eigenfunctions corresponding to a larger index.

The mass matrices for the eight-node element, the first to be generated, were calculated using Riemann-sum quadrature. Numerical convergence was slow. Convergence was estimated by comparing changes in element values, normalized with respect to the newly computed element, for increasing numbers of integration points. A 10^{-4} magnitude tolerance required the use of 10,800 points. With this large number of points, double precision arithmetic (about 19 decimal digits on the UNIVAC 1108) was required to control roundoff error.

Such slow convergence motivated the use of a Gauss-Legendre (GL) cartesian product quadrature rule [48] for the ten-node element. Convergence was significantly faster with this method. The 10^{-4} tolerance was met with a 64 x 64 point rule (4096 integration points).

Formulation and Programming Checks

Algorithm and programming accuracy were checked in two ways.

First, the $\underset{\sim}{M}_c$ matrix elements corresponding to the rigid body terms (which are the element area and polar moment of inertia about the crack tip) were identified and checked. Second, selected elements were evaluated in closed form and compared with the numerical results. In every case, agreement was reached.

The Eight-Node Element

The $\underline{C}$ vector and the $\underset{\sim}{f}$ matrices for the eight-node element are given in Table 2.1, along with a schematic matrix partition. The $\underline{C}$ vector arrangement was chosen to agree with [23,24]. This choice dictated the arrangement of the other matrices. The $\underset{\sim}{A}$ matrix also depends on nodal point ordering, which is that of [23,24] (Figure 2). The product matrices of equations (2.2) are shown in Tables 2-4. The $\underset{\sim}{A}$ matrix is shown in Table 5. In that Table, the notation $\underset{\sim}{f}_{mn}$ indicates the $\underset{\sim}{f}_m$ $(m = 1,2)$ matrix evaluated at the nth $(n = 1,2,\ldots 8)$ nodal point.

The Riemann sum quadrature algorithm was essentially:

1. Divide the element into square subareas and calculate the incremental area, $\Delta\bar{A}$.

2. Evaluate the $\underset{\sim}{f}_1$ and $\underset{\sim}{f}_2$ matrices at the center of each subarea.

3. Form the matrix products of equations (2.2) and multiply by $\Delta\bar{A}$.

4. Accumulate these incremental matrices - the sums being approximations to the required integrals.

The Ten-Node Element

The $\underline{C}$ vector and the $\underset{\sim}{f}$ matrices for the ten-node element are given in Table 6. The arrangement of the $\underline{C}$ vector, as for the eight-node element, agrees with that of [23]. From the table it is apparent that the symmetric coefficients are arranged first, and the antisymmetric coefficients last. The rigid body x-translation parameter $\bar{K}$ was placed in the symmetric part since x-translation is a symmetric displacement. Similarly, the rigid body y-translation parameter $\bar{H}$ and the rigid body rotation parameter $\bar{F}$ were placed with the antisymmetric coefficients. Since (equations (A54) - (A58b)) there is no antisymmetric Williams' eigenfunction corresponding to the eigenvalue $n = 2$ ($\bar{C}_{2a} \equiv 0$), that space was used for $\bar{H}$.

Because the ten-node element is square, a symmetric (equal number of function evaluation points in each coordinate direction) GL cartesian product quadrature rule was particularly easy to implement. In the coordinate system of Figure 1.3, the (nondimensionalized) element covers the unit square.

The function evaluation points (ordinates) for an n-point GL rule are the n roots of the nth order Legendre polynomial, which are symmetrically disposed about zero in the interval (-1,1). The weights associated with each ordinate (analogous to the $\Delta\bar{A}$ of the Riemann-sum rule), are all positive and also symmetric about zero.

In the GL algorithm used, the ordinates and weights were calculated rather than entered as data. A double precision version of a UNIVAC library routine was used. The ordinates agreed to 17 decimal digits and the weights to 16 decimal digits with the values of [46].

This approach markedly facilitated the convergence study and avoided errors in manual entry of many long numbers.

The GL cartesian product algorithm was essentially:

1. Calculate the ordinates and weights for the order operator desired.

2. For every y-ordinate, evaluate the $\underset{\sim}{f}_1$ and $\underset{\sim}{f}_2$ matrices at each x-ordinate.

3. Form the matrix products of equations (2.2) and multiply by the appropriate weights; for the (ith x-ordinate, jth y-ordinate) evaluation point, the appropriate weight is the product $W_i W_j$.

4. Accumulate these incremental matrices - the sums being approximations to the required integrals.

Confirmation Checks

During the entire process, accuracy and correctness checks were made where possible. The $\underset{\sim}{A}$ matrices were checked with those of [23,24]. Because of the way the computer program was written, this also checked much of the mass matrix integration program.

Further checks were made after the structural program was running. The elements' mass and polar moment of inertia were recovered, after the element matrices were dimensionalized and assembled by the structural program, by using the equation

$$2T = \underline{\hat{v}}^T \underset{\sim}{M} \underline{\hat{v}} = mv^2 \quad . \tag{2.3}$$

Here T is the kinetic energy, $\underline{\hat{v}}$ is the nodal point velocity vector and m is the total mass. For velocity vectors of unit magnitude, the

element mass was correctly recovered. A velocity field corresponding to rotation about the origin of coordinates with angular velocity ω,

$$\underline{\hat{v}}^T = w \lfloor -y \quad x \quad -y \quad x \quad -y \quad x \ldots \rfloor = \omega \underline{\hat{d}}^T \tag{2.4}$$

where $\omega = w/|\underline{\hat{d}}|$, gives

$$2T = \omega^2 \underline{\hat{d}}^T \underset{\sim}{\hat{M}} \underline{\hat{d}} = I_o \omega^2 \quad . \tag{2.5}$$

Here I_o is the moment of inertia about an axis normal to the plane of the element through the origin. For unit angular velocity, the elements' polar moment of inertia was recovered.

In addition, the ten-node element was used to predict natural frequencies for steel and aluminum plates with a crack (experimentally simulated by a narrow saw cut). The experimental results were obtained by Mr. John Malluck, a graduate student at the Georgia Institute of Technology. The steel plate experiment was conducted to define experiment parameters and technique. Results were reported in [50]. The aluminum plate experimental procedure and results were reported in detail in [35].

The entire steel plate was modeled by the ten-node element alone. Plate configuration and results are shown in Figure 4. The aluminum plate was modeled by the ten-node element alone and with the ten-node element as the central one-ninth of the plate, surrounded by constant strain triangles. The configurations, finite element results and experimental results are shown in Figure 5.

These results are significant in at least two respects. In the

first place, the close agreement of finite element and experimental results indicates that the high-order singularity element accurately represents the kinetic characteristics of a finite cracked plane elastic structure. Secondly, the close (within five percent) agreement between the crude (ten-node element alone) and refined model results for the aluminum plate implies that the high-order singularity element can be expected to produce accurate results from relatively coarse-grid finite element models.

Table 1. $\underline{C}$ Vector and $\underset{\sim}{f}$ Matrices for the Eight-node Element.

$$\underline{C}^T = \left[\bar{C}_{1s}\ \bar{C}_{2s}\ \bar{C}_{3s}\ \bar{C}_{4s}\ \bar{C}_{5s}\ \bar{C}_{6s}\ \bar{C}_{7s}\ \bar{C}_{8s}\ \bar{C}_{9s}\ \bar{C}_{10s}\ \bar{C}_{11s}\ \bar{C}_{12s}\ \bar{C}_{13s}\ \bar{K}\quad \bar{H}\quad \bar{F}\right]$$

$$\underline{f}_1 = \begin{bmatrix} \bar{u}_{1s}\ \bar{u}_{2s}\ \bar{u}_{3s}\ \bar{u}_{4s}\ \bar{u}_{5s}\ \bar{u}_{6s}\ \bar{u}_{7s}\ \bar{u}_{8s}\ \bar{u}_{9s}\ \bar{u}_{10s}\ \bar{u}_{11s}\ \bar{u}_{12s}\ \bar{u}_{13s}\ \cos\theta\ \sin\theta & 0 \\ \bar{v}_{1s}\ \bar{v}_{2s}\ \bar{v}_{3s}\ \bar{v}_{4s}\ \bar{v}_{5s}\ \bar{v}_{6s}\ \bar{v}_{7s}\ \bar{v}_{8s}\ \bar{v}_{9s}\ \bar{v}_{10s}\ \bar{v}_{11s}\ \bar{v}_{12s}\ \bar{v}_{13s}\ -\sin\theta\ \cos\theta & \bar{r} \end{bmatrix}$$

$$= \left[\begin{array}{c|c|c} \bar{u}_s & R & 0 \\ \hline \bar{v}_s & & \bar{r} \end{array}\right] = \left[\begin{array}{c|c|c} 1 \times 13 & 2 \times 2 & 1 \times 1 \\ \hline 1 \times 13 & & 1 \times 1 \end{array}\right]$$

$$\underline{f}_2 = \begin{bmatrix} \hat{u}_{1s}\ \hat{u}_{2s}\ \hat{u}_{3s}\ \hat{u}_{4s}\ \hat{u}_{5s}\ \hat{u}_{6s}\ \hat{u}_{7s}\ \hat{u}_{8s}\ \hat{u}_{9s}\ \hat{u}_{10s}\ \hat{u}_{11s}\ \hat{u}_{12s}\ \hat{u}_{13s}\ 0\ 0 & 0 \\ \hat{v}_{1s}\ \hat{v}_{2s}\ \hat{v}_{3s}\ \hat{v}_{4s}\ \hat{v}_{5s}\ \hat{v}_{6s}\ \hat{v}_{7s}\ \hat{v}_{8s}\ \hat{v}_{9s}\ \hat{v}_{10s}\ \hat{v}_{11s}\ \hat{v}_{12s}\ \hat{v}_{13s}\ 0\ 0 & 0 \end{bmatrix}$$

$$= \left[\begin{array}{c|c|c} \hat{u}_s & 0 & 0 \\ \hline \hat{v}_s & & 0 \end{array}\right] = \left[\begin{array}{c|c|c} 1 \times 13 & 2 \times 2 & 1 \times 1 \\ \hline 1 \times 13 & & 1 \times 1 \end{array}\right]$$

Table 2. Eight-node Element $\underset{\sim}{M}_{c_{11}}$ Integrand.

$\underline{f}_1^T \underline{f}_1 =$

$\left\{\bar{u}_s^T \; \bar{v}_s^T\right\} \begin{bmatrix} \bar{u}_s \\ \bar{v}_s \end{bmatrix}$	$\left\{\bar{u}_s^T \; \bar{v}_s^T\right\} \underset{\sim}{R}$	$\left\{\bar{v}_s^T\right\} \bar{r}$
	$\underset{\sim}{R}^T \underset{\sim}{R}$	$\begin{Bmatrix} -\sin\theta \\ \cos\theta \end{Bmatrix} \bar{r}$
symmetric		$\bar{r}^2$

Table 3. Eight-node Element $\underset{\sim}{M}_{c12}$ Integrand.

$\underline{f}_1^T\underline{f}_2 + \underline{f}_2^T\underline{f}_1 =$

$\left\{\bar{u}_s^T \ \bar{v}_s^T\right\}\begin{bmatrix}\hat{u}_s\\ \hat{v}_s\end{bmatrix} + \left\{\hat{u}_s^T \ \hat{v}_s^T\right\}\begin{bmatrix}\bar{u}_s\\ \bar{v}_s\end{bmatrix}$	$\left\{\hat{u}_s^T \ \hat{v}_s^T\right\}\underset{\sim}{R}$	$\left\{v_s^T\right\}\bar{r}$
symmetric	0	0
		0

Table 4. Eight-node Element $\underset{\sim}{M}_{c22}$ Integrand.

$\underline{f}_2^T \underline{f}_2 =$

$\begin{Bmatrix} \hat{u}_s^T & \hat{v}_s^T \end{Bmatrix} \begin{bmatrix} \hat{u}_s \\ \hat{v}_s \end{bmatrix}$	0	0
	0	0
symmetric		0

Table 5. Eight-node Element $\underset{\sim}{A}$ Matrix

$$\underline{A} = \underline{A}_1 + s\underline{A}_2$$

$$\underline{A} = \begin{bmatrix} f_{11} \\ f_{12} \\ f_{13} \\ f_{14} \\ f_{15} \\ f_{16} \\ f_{17} \\ f_{18} \end{bmatrix} + s \begin{bmatrix} f_{21} \\ f_{22} \\ f_{23} \\ f_{24} \\ f_{25} \\ f_{26} \\ f_{27} \\ f_{28} \end{bmatrix}$$

Table 6. Ten-node Element $\underline{C}$ Vector and $\underset{\sim}{f}$ Matrices.

$$\underline{C}^T = \left[\bar{C}_{1s}\ \bar{C}_{2s}\ \bar{C}_{3s}\ \bar{C}_{4s}\ \bar{C}_{5s}\ \bar{C}_{6s}\ \bar{C}_{7s}\ \bar{C}_{8s}\ \bar{C}_{9s}\ \bar{K}\quad \bar{C}_{12}\ \bar{H}\quad \bar{C}_{3a}\ \bar{C}_{4a}\ \bar{C}_{5a}\ \bar{C}_{6a}\ \bar{C}_{7a}\ \bar{C}_{8a}\ \bar{C}_{9a}\ \bar{F}\right]$$

$$\underset{\sim}{f}_1 = \begin{bmatrix} \bar{u}_{1s}\ \bar{u}_{2s}\ \bar{u}_{3s}\ \bar{u}_{4s}\ \bar{u}_{5s}\ \bar{u}_{6s}\ \bar{u}_{7s}\ \bar{u}_{8s}\ \bar{u}_{9s}\ \cos\theta\ u_{1a}\ \sin\theta\ \bar{u}_{3a}\ \bar{u}_{4s}\ \bar{u}_{5s}\ \bar{u}_{6s}\ \bar{u}_{7s}\ \bar{u}_{8a}\ \bar{u}_{9a}\ 0 \\ \bar{v}_{1s}\ \bar{v}_{2s}\ \bar{v}_{3s}\ \bar{v}_{4s}\ \bar{v}_{5s}\ \bar{v}_{6s}\ \bar{v}_{7s}\ \bar{v}_{8s}\ \bar{v}_{9s}\ -\sin\theta\ \bar{v}_{1a}\ \cos\theta\ \bar{v}_{3s}\ \bar{v}_{4a}\ \bar{v}_{5a}\ \bar{v}_{6a}\ \bar{v}_{7a}\ \bar{v}_{8a}\ \bar{v}_{9a}\ \bar{r} \end{bmatrix}$$

$$= \left[\begin{array}{c|c|c|c|c|c} \bar{u}_s & \cos\theta & \bar{u}_{1a} & \sin\theta & \bar{u}_a & 0 \\ \hline \bar{v}_s & -\sin\theta & \bar{v}_{1a} & \cos\theta & \bar{v}_a & \bar{r} \end{array}\right] = \left[\begin{array}{c|c|c|c|c|c} 1 \times 9 & 2 \times 1 & 2 \times 1 & 2 \times 1 & 1 \times 7 & 2 \times 1 \\ \hline 1 \times 9 & & & & 1 \times 7 & \end{array}\right]$$

$$\underset{\sim}{f}_2 = \begin{bmatrix} \hat{u}_{1s}\ \hat{u}_{2s}\ \hat{u}_{3s}\ \hat{u}_{4s}\ \hat{u}_{5s}\ \hat{u}_{6s}\ \hat{u}_{7s}\ \hat{u}_{8s}\ \hat{u}_{9s}\ 0\quad \hat{u}_{1a}\ 0\quad \hat{u}_{3a}\ \hat{u}_{4a}\ \hat{u}_{5a}\ \hat{u}_{6a}\ \hat{u}_{7a}\ \hat{u}_{8a}\ \hat{u}_{9a}\ 0 \\ \hat{v}_{1s}\ \hat{v}_{2s}\ \hat{v}_{3s}\ \hat{v}_{4s}\ \hat{v}_{5s}\ \hat{v}_{6s}\ \hat{v}_{7s}\ \hat{v}_{8s}\ \hat{v}_{9s}\ 0\quad \hat{v}_{1a}\ 0\quad \hat{v}_{3a}\ \hat{v}_{4a}\ \hat{v}_{5a}\ \hat{v}_{6a}\ \hat{v}_{7a}\ \hat{v}_{8a}\ \hat{v}_{9a}\ 0 \end{bmatrix}$$

$$= \left[\begin{array}{c|c|c|c|c|c} \hat{u}_s & 0 & \hat{u}_{1a} & 0 & \hat{u}_a & 0 \\ \hline \hat{v}_s & 0 & \hat{v}_{1a} & 0 & \hat{v}_a & 0 \end{array}\right] = \left[\begin{array}{c|c|c|c|c|c} 1 \times 9 & 2 \times 1 & 2 \times 1 & 2 \times 1 & 1 \times 7 & 2 \times 1 \\ \hline 1 \times 9 & & & & 1 \times 7 & \end{array}\right]$$

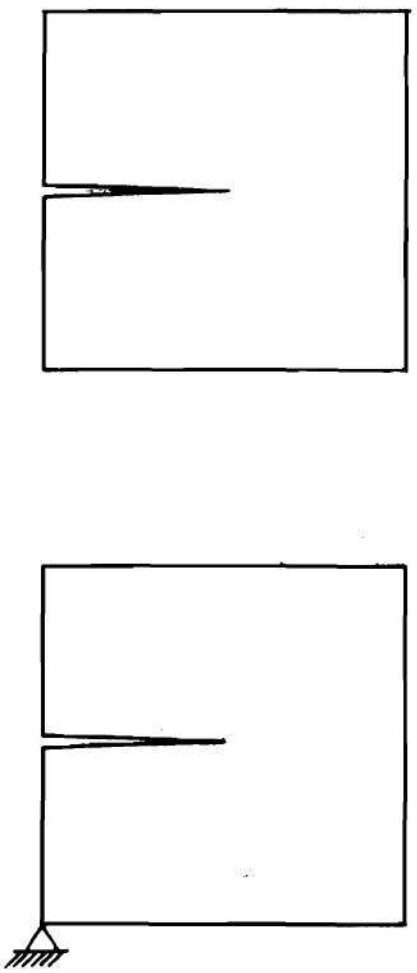

Steel Plate: 6 in. x 6 in. x 0.25 in.

Figure 4. Steel Plate Natural Frequencies.

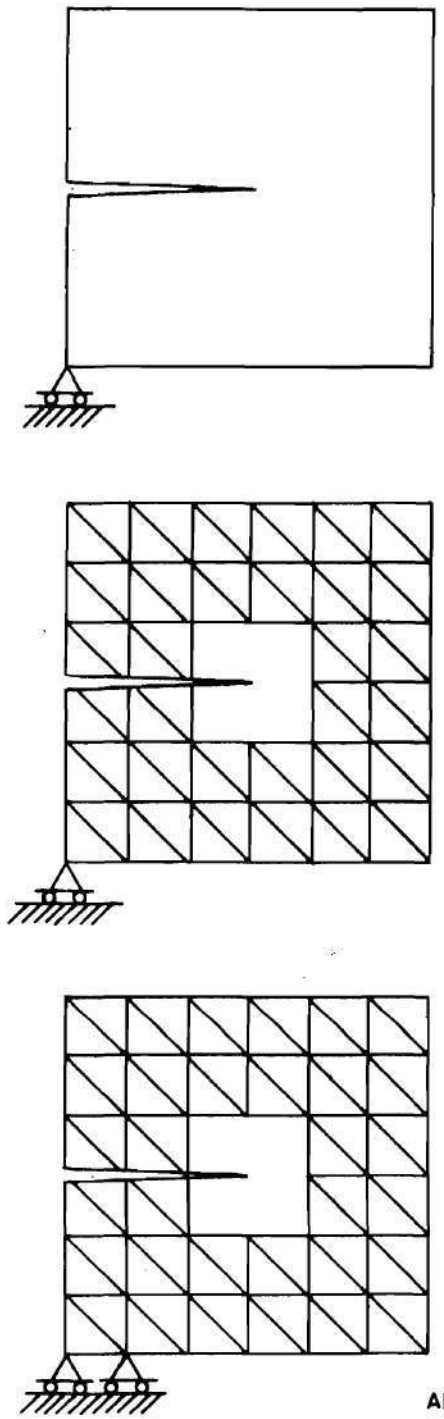

ALUMINUM PLATE: 6 IN. X 6 IN. X 0.50 IN.

Figure 5. Aluminum Plate Natural Frequencies.

CHAPTER III

PROBLEM SOLUTIONS

This chapter first briefly describes the structural computer program developed to incorporate the two cracked elements and then presents the results of two problem solutions. The first problem, a finite length crack opened by a suddenly applied uniform normal pressure [39,40], was chosen because it gave a direct check on results and because it provided a severe test of element performance. The second problem, an instrumented Charpy impact test [41,42,51], was chosen as representative of useful applications of a dynamic fracture analysis capability.

The Computer Program

The computer program used in this investigation was a research tool. Hence, simplicity and ease of modification rather than execution speed and economy were the primary considerations during its development. Even so problem solution times were relatively short. The program was written in UNIVAC 1108 FORTRAN V and designed for use from a remote terminal under the UNIVAC EXEC 8 operating system.

The program library is given in Table 7.

Due to the program's modular (driver-subroutine) organization, other elements can easily be added to the library.

The solutions available are shown in Table 8.

Table 7. Program Library.

Element	Mass	Stiffness
Eight-Node	X	X
Ten-Node	X	X
Constant Strain Triangle	X	X
Linear Spring		X
Point Mass	X	

Table 8. Solution Types.

Solution Type	Equation
Equilibrium	$\underset{\sim}{K}\underline{u} = \underline{F}$
Harmonic	$(\underset{\sim}{K} - \omega^2\underset{\sim}{M})\underline{u} = \underline{F}$
Transient	$\underset{\sim}{M}\ddot{\underline{u}} + \underset{\sim}{K}\underline{u} = \underline{F}(t)$

The solution type is specified during execution by input data. A crude determinant-search eigenvalue capability is incorporated into the harmonic analysis subroutine. This subroutine can be exercised as many times as desired, with different values of ω, during a run. The eigenvalues of $(\underset{\sim}{K} - \omega^2\underset{\sim}{M})$ are detected by very large displacement values accompanied by a phase shift. Although not economical, this method is simple and serviceable.

Every program function was checked and verified. The cracked element equilibrium solutions were checked against the values in [52-54]. Constant strain triangle mass and stiffness matrix formulation and assembly were verified by hand calculation, as was the equilibrium solution subroutine. The harmonic and transient solution subroutines were checked against hand calculations for various linear spring-lumped mass configurations. In every case, agreement was reached.

Crack Opened By Suddenly Applied Uniform Normal Pressure

Sih and Embley [39] and Sih, Embley and Ravera [40] reported the transient response of a finite length through crack in an infinite medium face loaded by a Heaviside step function normal pressure pulse. The results are presented as a plot of normalized stress intensity factor,

$$\bar{K}_I = K_I(\tau)/K_{Is} = \frac{\text{dynamic stress intensity factor}}{\text{equilibrium stress intensity factor}} \qquad (3.1)$$

versus nondimensionalized time,

$\tau = C_2 t/a$ = time/shear wave half-crack-length transit time. (3.2)

The equilibrium stress intensity factor for this problem [55] is

$$K_{Is} = p(\pi a)^{\frac{1}{2}} , \tag{3.3}$$

where p is the crack face pressure. C_2, the shear (distortional) wave speed, is related to the material shear modulus G and mass density ρ by

$$C_2 = (G/\rho)^{\frac{1}{2}} . \tag{3.4}$$

A comparison of the finite-element and analytic results is shown in Figure 7.

The Finite-Element Model

The problem solved in [39], and the finite element model used in this investigation are depicted in Figure 3.1. Because of symmetry only a quarter of the continuum was modeled. The material properties are given in Table 9.

Table 9. Sih Problem Material Properties.

Material Property	Value	Units
E	2.9×10^{7}	lb/in^2
ν	0.292	
ρ	7.3×10^{-4}	$lb\text{-}sec^2/in^4$

The Poisson's ratio of 0.292 was determined by the wave speed ratio,

$$\varkappa = C_2/C_1 = 0.542 \ , \tag{3.5}$$

used in [39]. In (3.5) C_1 is the dilatational wave speed. $\varkappa$ is related to Poisson's ratio by

$$\varkappa^2 = (1 - 2\nu)/2(1 - \nu) \tag{3.6a}$$

or

$$\nu = (1 - 2\varkappa^2)/2(1 - \varkappa^2) \ . \tag{3.6b}$$

The values for E and ρ are typical for steel. Finite element model parameters are given in Table 10.

Table 10. Sih Problem Model Parameters.

Parameter	Value	Units
Thickness	1.0	inch
Crack Half-Length	10	inch
Model Radius	60	inch
Numerical Integration Time Step Size	2.0163	microsecond
C_2	0.124	in/microsecond
C_1	0.229	in/microsecond

Model Response

There were three major sources of discrepancy between the finite element solution and the infinite continuum solution of [39].

The most obvious of these is that the finite element model, necessaryily, was of finite size. Thus, the stress intensity factor produced by the finite element model was expected to differ from the analytical solution value after boundary-reflected waves returned to the crack tip region. The finite-element model was sized so that the initial part of the $\bar{K}_1$ - τ curve was not influenced by reflections. The effect of the reflected waves was investigated by running the problem with the remote boundary first free and then fixed. As expected, the results were identical until the first reflected wave returned to the crack tip, after which the fixed boundary results show the effects of the reflected tensile waves, while the free boundary results show the effects of the reflected compressive waves. The arithmetic average of the remote-boundary-fixed and the remote-boundary-free results falls closely on the analytical solution. Apparently, the model was large enough for the crack to appear to the boundary as a point wave source, for which superposition of the two boundary conditions is equivalent to the unbounded medium response.

Some of the finite element solution parameters are given in Table 11.

A second source of discrepancy between the continuum and finite-element results is the wave front "smear-forward" inherent in the discrete model. Elements ahead of the wave front, which should be unaffected, have some "foreknowledge" of the approaching wave.

Table 11. Sih Problem Solution Times.

Parameter	Remote Boundary Free	Remote Boundary Fixed
Degrees of Freedom	156	144
Number of Time Steps	400	400
Total Computer Time	129.5 sec	120.4 sec

This effect, readily apparent in the graphical presentation of finite element results (Figure 7), appears as an oscillation in nodal point displacement, and hence as noise in the stress intensity factor response. As mentioned in Chapter 1, some of the response irregularity preceeding a wave can be reduced by using a diagonalized mass matrix. This smoother initial response, judging from the results of [30], is obtained at the expense of a less accurate representation of wave front slope and rise time, and more erratic displacement values behind the wave front. The wave forms in [30] indicate that use of a diagonal mass matrix results in filtering out some of the higher frequency displacement components.

A third source of error in this problem was application of the nodal forces representing the crack face pressure pulse only to crack face nodes. This procedure was simple to implement, but did not maintain the "consistent" approach used for generation of the mass matrix. The consistent nodal loads corresponding to any crack face traction distribution can be readily computed from equations (B15b) and (B15d) of Appendix B, using the $\underset{\sim}{f}_1$ and $\underset{\sim}{f}_2$ matrices. The $\underset{\sim}{f}$ matrix

construction is shown in Table 1.

The $\underline{F}_{sc}$ (surface traction consistent load vector with respect to the generalized coordinates) vector corresponding to a uniform crack face normal pressure was calculated analytically. The $\underline{F}_{sc}$ components corresponding to even subscripted Williams' series coefficients were all zero, while those corresponding to odd subscripted coefficients were all of the same order to magnitude. The $\underline{F}_{sc}$ components corresponding to the rigid body motion coefficients were an order of magnitude smaller.

As is evident from equation (B15b), transformation of $\underline{F}_{sc}$ into $\underline{F}_{s}$ (surface traction consistent load vector with respect to the nodal displacements) would result generally in a full (no zero components) vector. This result is interesting in at least two respects. First, it illustrates that the condition for interelement compatibility (that the element edge displacements be a function only of the nodal displacements along that edge) is also the necessary condition for consistent nodal loads corresponding to a loaded edge to appear only at the nodes along that edge. That is, it shows that one of the consequences of using an incompatible element is that the consistent surface traction load vector may explicitly introduce nodal loads at nodes other than on the loaded face, and thus at nodes in the interior of the modeled continuum. This effect is some sense compounds the "infinite wave speed" effect inherent in the discretized model. Secondly, the consistent nodal load vector corresponding to a uniform crack face normal pressure has both x and y components, while the normal pressure is statically equivalent to a force in the y direction.

These effects were not intuitively obvious, at least when that intuition was developed in dealing with constant strain triangle and other simple elements.

Comparison of K_{Is} values for crack face nodes loaded and for remote boundary nodes loads showed that the crack-face loaded K_{Is} values were inaccurate. Typically, errors of 20 to 40 percent were found, depending on the way the loads were distributed among the crack face nodes. The remote-boundary loaded K_{Is} value, on the other hand, was within 2.5 percent of the finite width sheet value of Isida [54].

The load distribution used for obtaining the results shown in Figure 3.2 was the one corresponding to the crack face nodal point reactions when those nodes were restrained against vertical deflections with the remote boundary loaded. Other crack-face-node load distributions were tried during the course of the investigation. Varying the distribution resulted in different K_{Is} values, slightly affected the initial shape of the $\bar{K}_I - \tau$ curve, and gave slightly different maximum values of $\bar{K}_I(\tau)$. The overall $\bar{K}_I - \tau$ response was essentially the same for each case.

The results of the finite element solutions are graphically compared with those of [39] in Figure 7. As is evident, the agreement is excellent.

Instrumented Charpy Impact Test

Efforts to correlate instrumented Charpy impact test [41] data with other fracture toughness test data and with service experience

have a long and for the most part unsuccessful history [42]. Recent efforts [42,43,51] have met with more success. As discussed in [42], elastic fracture mechanics had little applicability to this area prior to the use of modified (sidegrooved, pre-cracked, sidegrooved and pre-cracked) specimens, because most test failures were due to gross yielding and involved much plastic flow. The fracture phenomena of interest in service, on the other hand, were largely below-yield (brittle) fractures, to which elastic fracture mechanics concepts apply. Modified Charpy specimens more frequently fail in a brittle manner, and their low cost and ease of handling provided strong motivation for fracture toughness correlation efforts.

The simple approach of using the peak tup load in the three-point bend formula [53], with inertia effect corrections based on beam theory [42,51,56], produced fairly good results. The analog computer model of [43] gave nearly quantitative agreement with experiment and showed conclusively that there was no simple relation between tup load, specimen effective load and anvil load. Consequently, simplistic correlation attempts were strongly liable to error.

The instrumented Charpy test problem was chosen as an example of a practical and useful application of the cracked structure dynamic analysis capability afforded by the singularity elements. That is, it was expected that the finite element model could be used to give an accurate value of fracture toughness (K_{IC}) based on tup load-time and specimen time- to-fracture records from the Charpy test of a specimen which failed in a brittle fracture mode. The finite element model

K_I-time results are shown in Figure 10.

Assumptions and Simplifications

A examination of published data [42,51,57] showed that the tup load-time records of Charpy tests in which the specimen failed by brittle fracture were characterized by a nominally triangular or half-sinusoidal shape. To simplify programming, triangular and half sinusoidal force inputs were used in the analysis. Of course, in application, the actual load-time trace would be used. Provision for this was made in the program.

The gage lengths of the strain gages used to measure the tup load, in those tests for which information was available, were so large compared to the tup dimensions that the tup load-time curve could be considered as the spatially averaged effect of the rest of the striker head on the tup/specimen assembly. Using this rationale, only the tup tip, back to approximately the strain gage centerline, was modeled. Since the elastic waves involved in the force transmission have a finite wave speed, the applied load onset was delayed by an amount of time representing wave transit time from the strain gage centerline to the tup tip.

In the absence of reported values of initial impact velocity, the impact velocity for the problem was chosen as 15 feet per second which is in the middle of the ASTM standard [41] allowable range.

The Finite Element Model

Dimensional specifications from [41] for the Type A Charpy specimen and for the impact test are shown in Figure 8. The finite element model and the tup load-time curve used are shown in Figure 9.

Due to symmetry, only half the specimen and tup tip was modeled. The anvil support condition was enforced by fixing the node corresponding to the point in contact with the anvil edge. The relatively small singularity element size was due solely to the attempt to model the notch. It is most likely that a much larger singularity element would provide adequate results. For convenience, the tup and specimen were taken to be of the same material. In practice, of course, this would not necessarily be the case. The program can easily handle any combination of materials.

The material properties are given in Table 12.

Table 12. Charpy Problem Material Properties.

Material Property	Value	Unit
E	2.07×10^{10} 3.0×10^{7}	$dynes/mm^2$ lb/in^2
ν	0.25	
ρ	8.34×10^{-4} 7.8×10^{-4}	$dyne\text{-}sec^2/mm^4$ $lb\text{-}sec^2/in^4$

Other model parameters of interest are given in Table 13.

The computer solution for $K_I(t)$ is shown in Figure 10. The run parameters are given in Table 14.

Results

A significant feature of the $K_I(t)$ - t curve is the dive to negative values during the first two microseconds after impact. The

Table 13. Charpy Problem Model Parameters.

Parameter	Value	Unit
Precrack Depth	0.25	millimeter
Tup Initial Velocity	4.572×10^3 15	mm/sec ft/sec
Load Onset Delay	3	microsecond
Load Pulse Width	50	microsecond
Load Amplitude	1.512×10^9 3400	dynes pounds
C_2	1.99	mm/sec
C_1	3.45	mm/sec

Table 14. Charpy Problem Solution Times.

Degrees of Freedom	225
Number of Time Steps	600
Total Computer Time	215.39 sec

negative stress intensity factor reflects the crack-closing compressive stress wave which initially propagates through the specimen. Until this wave is reflected from the notched side of the specimen as a tension wave, the crack is closed. This effect demonstrates rather conclusively the cracked elements' sensitivity to wave phenomena. Subsequently, the crack-opening effect dominates, and the stress intensity factor increases rapidly.

In agreement with the load-time variation reported in [43], the stress intensity factor increases with time in a sensibly linear manner. When the tup load has peaked, $K_I(t)$ had not quite reached the equilibrium K_{Is} for the load, while the peak $K_I(t)$ occurred at about the time the tup load had fallen back to zero. These results reinforce the conclusions of [42] concerning the importance of dynamic effects in the Charpy test.

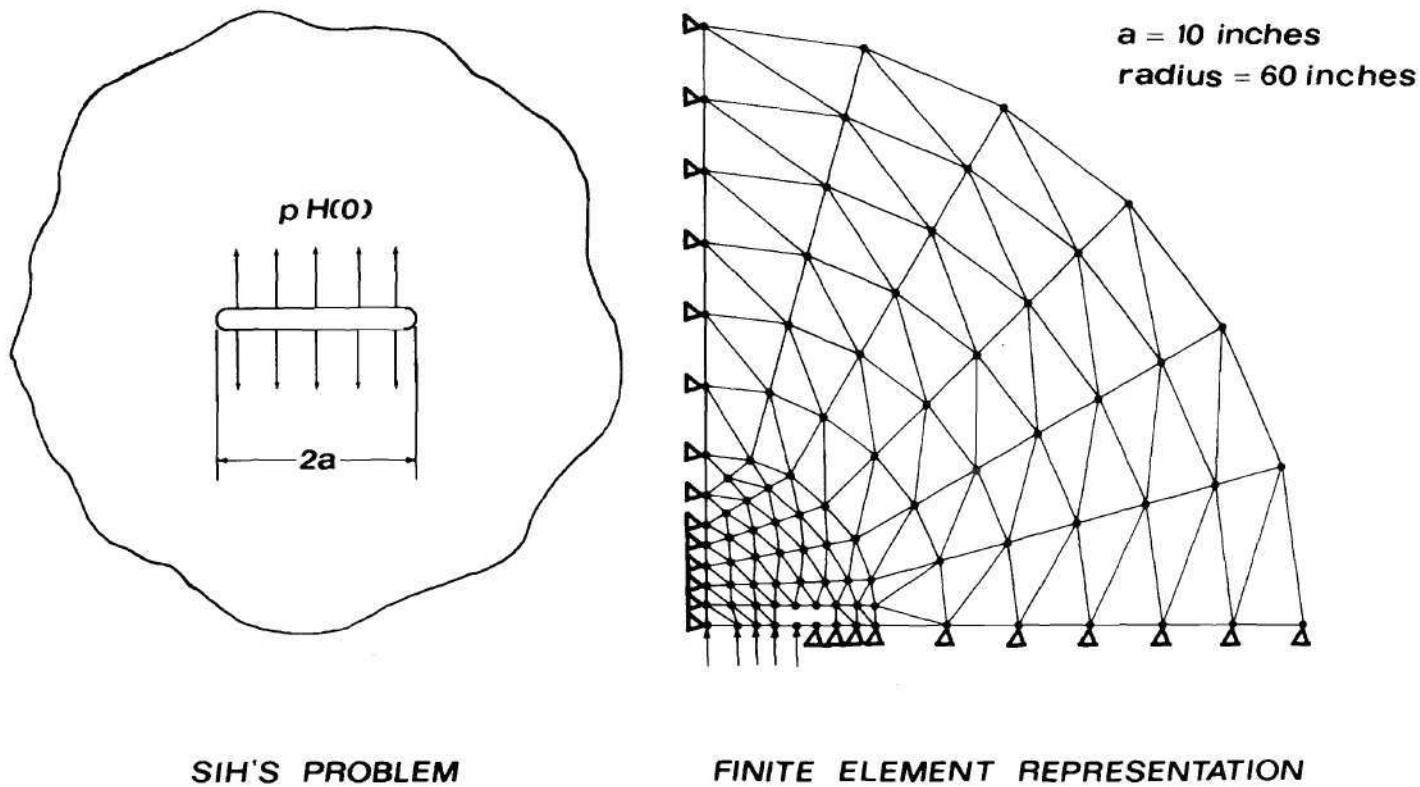

Figure 6. Sih Problem Finite Element Model.

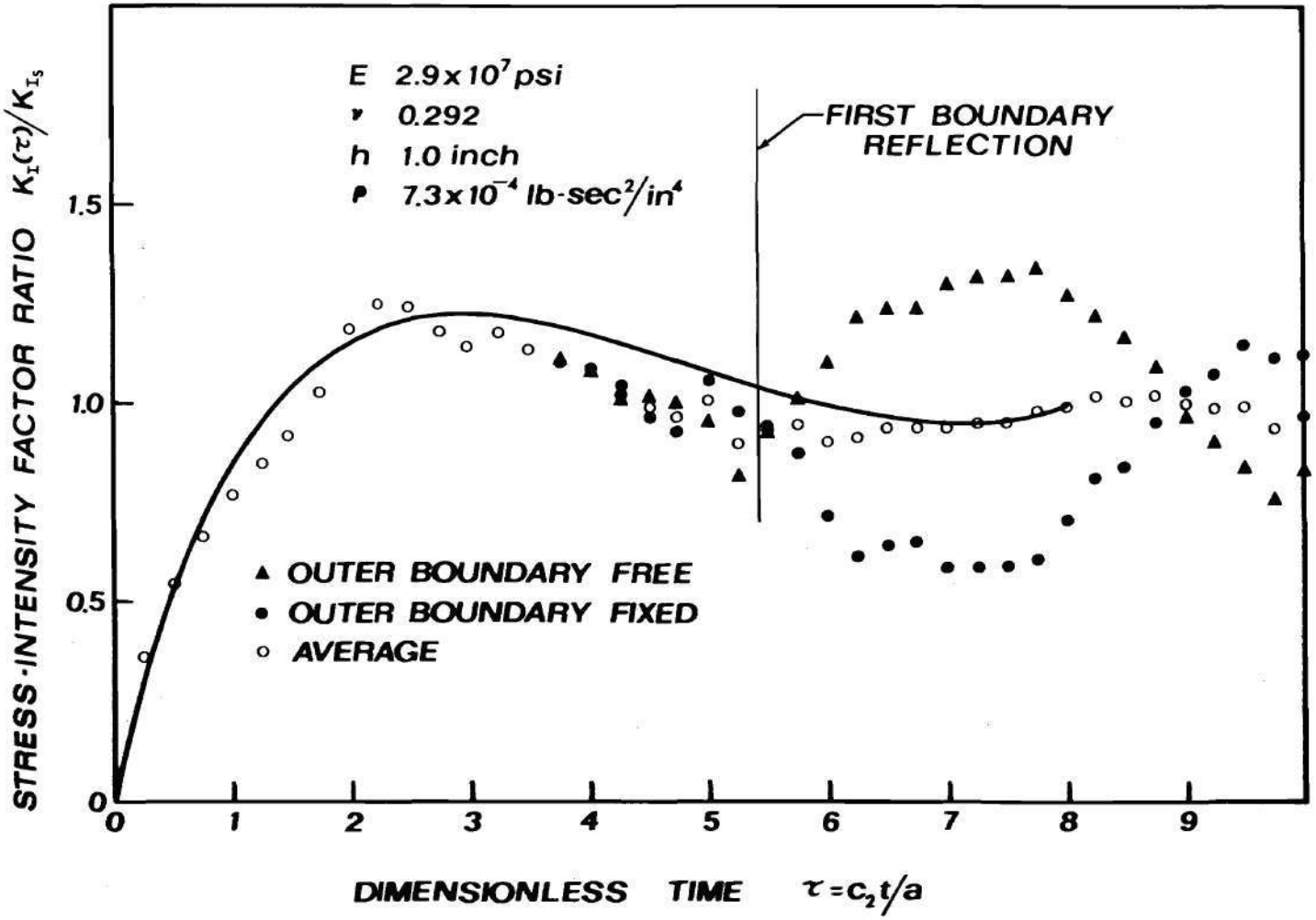

Figure 7. Sih Problem Results.

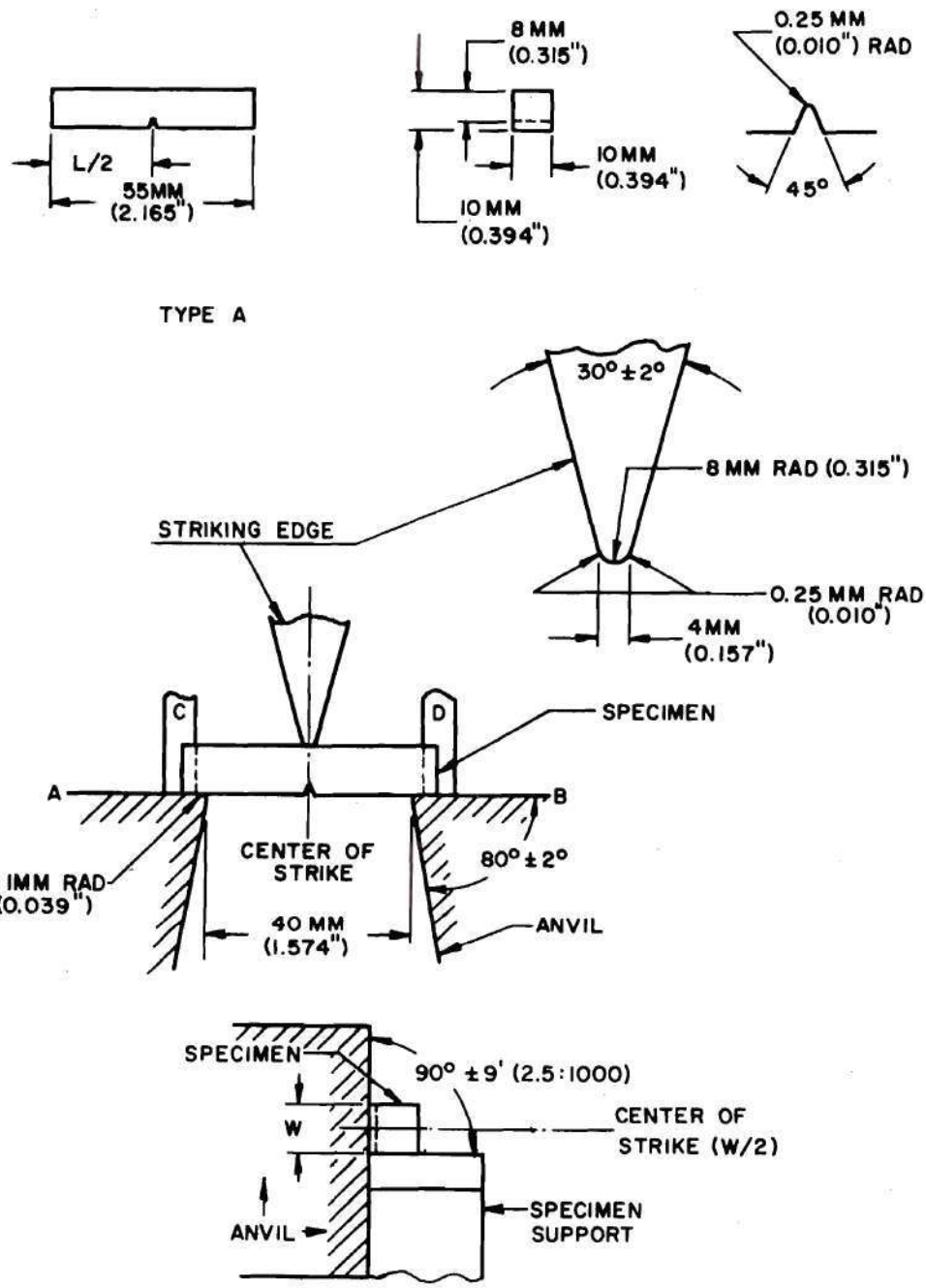

Figure 8. Charpy Specimen and Test Specifications.

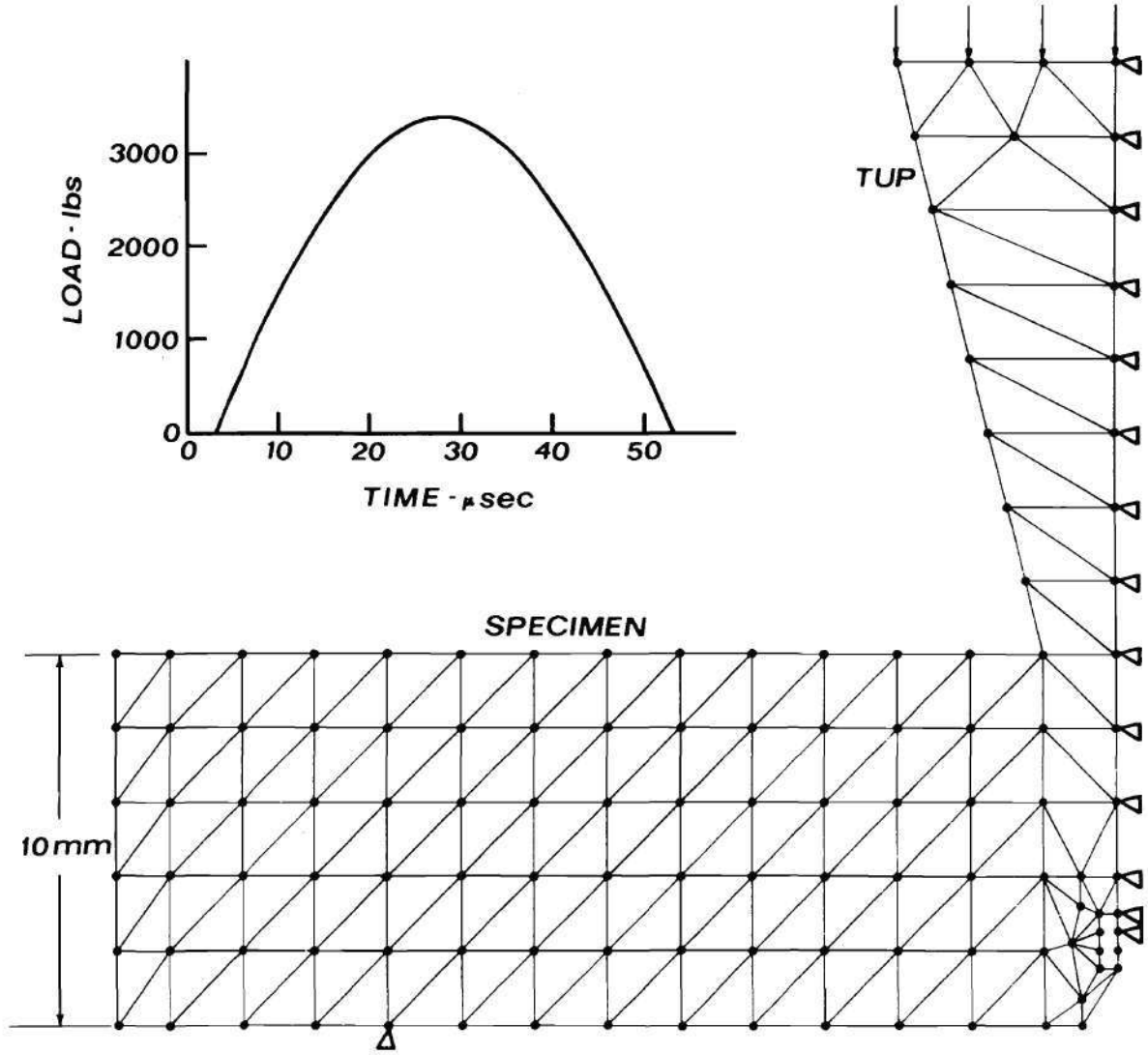

FINITE ELEMENT REFRESENTATION OF CHARPY SPECIMEN

Finite 9. Charpy Load and Finite Element Model.

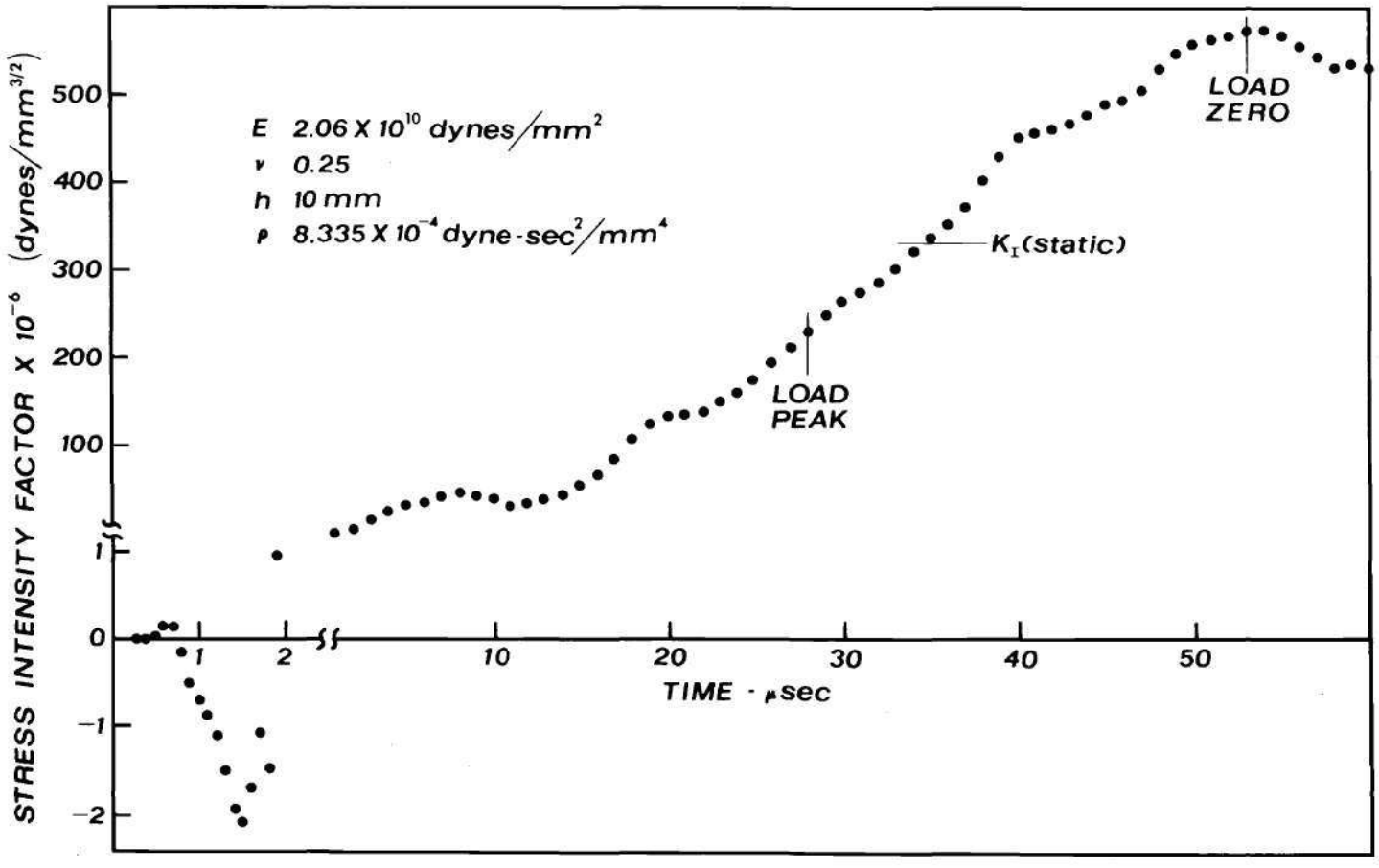

Figure 10. Charpy Results.

CHAPTER IV

DISCUSSION AND CONCLUSIONS

The dynamic capability developed in this work is a unique advance in the analysis of cracked plane structures. It provides a rational, rigorous and accurate solution method for heretofore intractable problems.

The high-order elements consistent mass matrices, which are the primary contribution, were constructed by the generalized coordinate method. The displacement coordinate functions were selected from the Williams' series of eigenfunctions for a stress-free crack. Rigid body terms were included.

The computer program developed to use the elements is capable of equilibrium, harmonic excitation, eigenvalue and undamped transient response solutions for plane cracked structures which can be modeled by a combination of cracked elements, constant strain triangles, linear springs and point masses. The modular construction of the program allows easy addition of other elements to the library and also permits easy addition of other functional modules.

The equilibrium solution capability was checked against established values for particular configurations. In every case agreement was excellent. The high-order elements removed the need for highly detailed models with very significant economies in data preparation and problem execution time compared to previous finite element solutions.

The harmonic response analysis capability was used in its recursive mode to predict the natural frequencies of steel and aluminum square cracked plates. The predicted frequencies agreed closely with experimentally determined frequencies. The models used, as for the equilibrium problems, had relatively few degrees of freedom and were very economical to construct and to run.

The transient response analysis capability was checked against Sih and Ravera's transform method solution. The finite element model results were in excellent agreement with the analytic solution.

As an example of a potential production application of the high-order cracked element dynamic capability, an instrumented Charpy impact test was modeled. The finite element results were in close agreement with recent analog computer results. This indicates a real potential for economical and quick fracture toughness determination by using detailed tup load-time and time-to-fracture records from brittle fracture Charpy tests "interpreted" by a finite-element model.

The mass matrix generation programs could be considerably simplified and slightly speeded up by adoption of the formulation of equations (A26) rather than (A27). This change would avoid some zero denominators which in the present formulation require interruption of the orderly calculation of the $\underset{\sim}{f}$, $\underset{\sim}{K}_c$, $\underset{\sim}{M}_c$, and $\underset{\sim}{A}$ matrices.

Some considerations which were not critical in this investigation are nevertheless worthy of further investigation.

The matter of high-order singularity element optima should be on some interest. In view of the opinion of Tong and Pian that the special element size should not be too small in comparison to the

crack length, there may be an optimum high-order element size for a given grid. There is no a priori reason to believe that the element shapes used in this investigation are optimum. A study of the effects of changes in accuracy with element height/width aspect ratio might prove fruitful. By the same token, the number of degrees of freedom, and hence the number of element nodal points, may be significant to accuracy. An increase in element complexity as reflected in a greater number of degrees of freedom is usually accompanied by increased model bandwidth and thus increased computation cost. The tradeoff between element complexity, model refinement and computation costs would certainly be of interest to a "production" user of the elements.

In the elements developed for this investigation, there is a one-to-one correspondence between nodal displacement degrees of freedom and generalized coordinates. This relationship is not essential and more Williams' eigenfunctions, or other functions, could be built into the element by using internal nodes in the element formulation. These nodes could be eliminated by the usual condensation process, should bandwidth be excessive. Alternatively, the present elements, which are possibly too flexible, might benefit from fewer degrees of freedom, with the nodal displacements correlated with the generalized coordinates by the least squares technique.

A diagonalized mass matrix for the high order cracked element would be very useful for several reasons. There is, of course, the resulting reduction in storage. Additionally, the diagonal mass matrix would enable use of an explicit time integration algorithm, with probable savings in problem run times for some problems. The

diagonal mass matrix could be of some benefit in wave propagation problems. In these problems it should show a smoother wave shape without the oscillations frequently apparent in consistent mass results. The question of an accurate and rational diagonalization method certainly warrants further investigation.

Finally, as pointed out by Williams, the stress function approach can be applied to elementary plate theory for bending analysis of a cracked plate [16]. Given the displacement eigenfunctions appropriate to the bending problem, construction of a plate-bending high-order singularity element is straightforward.

Such an element is of obvious utility for sonic fatigue, for plates loaded by transverse blast waves and for projectile impact problems. Most likely elementary plate theory will be inadequate for such an element, since the boundary radius of curvature near the crack tip is small relative to plate thickness. As discussed by Timoshenko and Woinowsky-Krieger [66], elementary plate theory is usually inaccurate in regions where the transverse shear stresses are of major importance. Whether a higher-order plate theory will yield results comparable in utility to those for plane extension remains to be seen.

APPENDIX A

THE WILLIAMS' SERIES

The displacement coordinate functions used in this investigation are developed in this appendix.

Stress Eigenfunctions

Fortuitously, a stress function of the form

$$\Phi_\lambda = r^{\lambda+1} f(\theta) \tag{A1}$$

will satisfy the governing differential equation,

$$\nabla^4 \Phi = 0 \ , \tag{A2}$$

and the free crack face boundary conditions

$$\sigma_{\theta\theta} = 0 \ ; \quad \sigma_{r\theta} = 0 \ ; \quad \text{at } \theta = \pm \pi \ . \tag{A3}$$

The ∇^4 operator may be written

$$\nabla^4 = \nabla^2 \nabla^2 \ . \tag{A4a}$$

In plane polar coordinates

$$\nabla^2(\ ) = r^{-1}(\partial/\partial r(r(\partial/\partial r(\ ))) + r^{-2}(\partial^2/\partial r^2(\ )) \ . \tag{A4b}$$

Substitution of the stress function (A1) into the biharmonic equation (A2) yields the ordinary differential equation for $f(\theta)$,

$$(D_\theta^2 + (\lambda + 1)^2)(D_\theta^2 + (\lambda - 1)^2)f(\theta) = 0 \ , \tag{A5}$$

where $D_\theta = d/d\theta$. Equation (A5) has the general solution*

$$f(\theta) = C_{\lambda 1}S(\lambda + 1)\theta + C_{\lambda 2}C(\lambda + 1)\theta$$

$$+ C_{\lambda 3}S(\lambda - 1)\theta + C_{\lambda 4}C(\lambda - 1)\theta \ , \tag{A6}$$

where S has been written for sin, C for cos and the four integration constants have been designated $C_{\lambda 1} - C_{\lambda 4}$. Thus, the stress function (A1) can be written as

$$= r^{\lambda - 1}(C_{\lambda 1}S(\lambda + 1)\theta + C_{\lambda 2}C(\lambda + 1)\theta$$

$$+ C_{\lambda 3}S(\lambda - 1)\theta + C_{\lambda 4}C(\lambda - 1)\theta \ . \tag{A7}$$

From (A7), via the usual stress-stress function relations [30],

$$\sigma_{rr} = r^{-1}(\partial/\partial r(\Phi)) + r^{-2}(\partial^2/\partial\theta^2(\Phi)) \ , \tag{A8a}$$

$$\sigma_{\theta\theta} = \partial^2/\partial r^2(\Phi) \ , \tag{A8b}$$

and

$$\sigma_{r\theta} = - (\partial/\partial r(r^{-1}(\partial/\partial\theta(\Phi))) \ , \tag{A8c}$$

the stresses are

$$\sigma_{rr} = r^{\lambda-1}(f''(\theta) + (\lambda + 1)f(\theta)) \tag{A9a}$$

*In (A6) the values $\lambda = 0, \pm 1$ produce special solutions. These will be considered subsequently.

$$\sigma_{\theta\theta} = \lambda(\lambda + 1)r^{\lambda - 1}f(\theta) \tag{A9b}$$

and

$$\sigma_{r\theta} = -\lambda r^{\lambda - 1}f'(\theta) \quad . \tag{A9c}$$

The boundary conditions (A3) then require

$$f(\pm \pi) = 0 \tag{A10a}$$

and

$$f'(\pm \pi) = 0 \quad . \tag{A10b}$$

These boundary conditions, applied to equation (A7), give

$$C_{\lambda 1}S\alpha\pi + C_{\lambda 2}C\alpha\pi + C_{\lambda 3}S\beta\pi + C_{\lambda 4}C\beta\pi = 0 \ , \tag{A11a}$$

$$-C_{\lambda 1}S\alpha\pi + C_{\lambda 2}C\alpha\pi - C_{\lambda 3}S\beta\pi + C_{\lambda 4}C\beta\pi = 0 \ , \tag{A11b}$$

$$\alpha C_{\lambda 1}C\alpha\pi - \alpha C_{\lambda 2}S\alpha\pi + \beta C_{\lambda 3}C\beta\pi - \beta C_{\lambda 4}S\beta\pi = 0 \tag{A11c}$$

and

$$\alpha C_{\lambda 1}C\alpha\pi + \alpha C_{\lambda 2}S\alpha\pi + \beta C_{\lambda 3}\beta\pi + \beta C_{\lambda 4}S\beta\pi = 0 \ , \tag{A11d}$$

in which the notation

$$\alpha = \lambda + 1 \quad \text{and} \quad \beta = \lambda - 1 \tag{A12}$$

has been introduced.

Simple additions and subtractions of equations (A11) lead to

$$C_{\lambda 2}C\alpha\pi + C_{\lambda 4}C\beta\pi = 0 \ , \tag{A13a}$$

$$\alpha C_{\lambda 2}S\alpha\pi + \beta C_{\lambda 4}S\beta\pi = 0 \ , \tag{A13b}$$

and

$$C_{\lambda 1}C\alpha\pi + C_{\lambda 3}S\beta\pi = 0 \ , \tag{A14a}$$

$$\alpha C_{\lambda 1}C\alpha\pi + \beta C_{\lambda 3}C\beta\pi = 0 \ , \tag{A14b}$$

from which it is apparent that the eigenfunction problem separates naturally into symmetric (A13) and antisymmetric (A14) parts.

The relationship between α and β (A12), along with the periodicity of circular functions, gives

$$S\alpha\pi = S(\beta + 2)\pi = S\beta\pi \tag{A15a}$$

and

$$C\alpha\pi = C(\beta + 2) = C\beta\pi \ , \tag{A15b}$$

so that (A13) and (14) may be written as

$$C_{\lambda 2}C\alpha\pi + C_{\lambda 4}C\alpha\pi = 0 \ , \tag{A16a}$$

$$\alpha C_{\lambda 2}S\alpha\pi + \beta C_{\lambda 4}S\alpha\pi = 0 \tag{A16b}$$

and as

$$C_{\lambda 1}S\alpha\pi + C_{\lambda 3}S\alpha\pi = 0 \ , \tag{A17a}$$

$$\alpha C_{\lambda 1}C\alpha\pi + \beta C_{\lambda 3}C\alpha\pi = 0 \tag{A17b}$$

respectively.

Equations (A16) and (A17) have the same characteristic equation

$$\alpha S\alpha\pi C\alpha\pi - \beta S\alpha\pi C\alpha\pi = 0 \ . \qquad \text{(A18)}$$

Hence the eigenvalues are the same for both parts of the problem. Equation (A18) reduces by trigonometric identity to

$$\sin(2\lambda\pi) = 0 \ , \qquad \text{(A19)}$$

so that the eigenvalues (including some that are physically inadmissible) are

$$\lambda = n/2 \qquad \text{(A20)}$$

for $n = 0, \pm 1, \pm 2, \ldots$.

The two constants associated with each mode can now be related. In terms of the eigenvalues (A20), equations (A16) become

$$(C_{n2} + C_{n4})\cos(n/2 + 1) = 0 \qquad \text{(A21a)}$$

and

$$[(n/2 + 1)C_{n2} + (n/2 - 1)C_{n4}]\sin(n/2 + 1) = 0 \ , \qquad \text{(A21b)}$$

where the constants $C_{\lambda m}$ have been renamed C_{nm}. For even n, equation (A21a) requires

$$(C_{n2} + C_{n4}) = 0 \ , \qquad \text{(A22a)}$$

while (A21b) is identically satisfied. Similarly, for odd n equation (A21b) requires

$$(n/2 + 1)C_{n2} + (n/2 - 1)C_{n4} = 0 \ , \tag{A22b}$$

while (A21a) is identically satisfied. These equations can be consolidated into

$$(n/2 + 1)C_{n2} + (n/2 + (-1)^n)C_{n4} = 0 \ . \tag{A23}$$

In the same manner, equations (A17) lead to the relation

$$(n/2 + 1)C_{n1} + (n/2 - (-1)^n)C_{n3} = 0 \ . \tag{A24}$$

Using relations (A23) and (A24), the stress eigenfunctions may be written as

$$\Phi_n(r,\theta) = r^{(n/2 + 1)}(f_{an}(\theta) + f_{sn}(\theta)) \ , \tag{A25}$$

where

$$f_{an}(\theta) = C_{na}[-((n/2 - (-1)^n)/(n/2 + 1))\sin(n/2 + 1)\theta + \sin(n/2 - 1)\theta] \tag{A26a}$$

and

$$f_{sn}(\theta) = C_{ns}[-((n/2 + (-1)^n)/(n/2 + 1))\cos(n/2 + 1)\theta + \cos(n/2 - 1)\theta] \tag{A26b}$$

are respectively the antisymmetric and symmetric parts of $f(\theta)$. Of course, (A26) is not the only representation possible. This form results when constants C_{3n} and C_{4n} are retained, and the constants C_{1n}

and C_{2n} replaced by use of (A23) and (A24). If C_{1n} and C_{2n} are retained instead, there results

$$f_{an}(\theta) = \hat{C}_{na}[\sin(n/2 + 1)\theta - ((n/2 + 1)/(n/2 - (-1)^n)\sin(n/2 - 1)\theta] \quad \text{(A27a)}$$

and

$$f_{sn}(\theta) = \hat{C}_{ns}[\cos(n/2 + 1)\theta - ((n/2 + 1)/(n/2 + (-1)^n))\cos(n/2 - 1)\theta] . \quad \text{(A27b)}$$

Displacement Eigenfunctions

The labor involved in constructing the displacement functions can be considerably reduced because each term of a given eigenfunction is itself a stress function. In what follows

$$s = \begin{cases} \nu \text{ (Poisson's ratio)} & \text{for plane strain} \\ \nu/(1 + \nu) & \text{for plane stress} \end{cases} \quad \text{(A28)}$$

and G is the shear modulus.

The constitutive relations for plane elasticity are

$$2G\epsilon_{rr} = (1 - s)\sigma_{rr} - s\sigma_{\theta\theta} , \quad \text{(A29a)}$$

$$2G\epsilon_{\theta\theta} = (1 - s)\sigma_{\theta\theta} - s\sigma_{rr} \quad \text{(A29b)}$$

and

$$2G\epsilon_{r\theta} = 2\sigma_{r\theta} . \quad \text{(A29c)}$$

The strain-displacement equations, slightly rearranged, are

$$\partial/\partial r(2Gu_r) = 2G\epsilon_{rr} \quad , \tag{A30a}$$

$$\partial/\partial\theta\ (2Gv_\theta) = r(2G\epsilon_{\theta\theta}) - 2Gu_r \tag{A30b}$$

and

$$2G\epsilon_{r\theta} = r^{-1}(\partial/\partial\theta\ (2Gu_r)) + r(\partial/\partial r\ (r^{-1}2Gu_\theta)) \quad . \tag{A30c}$$

The symmetric terms of the stress function are of the form

$$\Phi_{sn} = r^{\alpha} \cos\beta\theta \ , \tag{A31}$$

where α and β are related by

$$\alpha = \lambda + 1 \tag{A32a}$$

and

$$\beta = \lambda + 1 \ ; \quad \beta = \lambda - 1 \ , \tag{A32b}$$

so that the conditions

$$\alpha^2 = \beta^2 \tag{A32c}$$

or

$$(\alpha - 2)^2 = \beta^2 \ , \tag{A32d}$$

necessary for (A31) to satisfy the biharmonic equation, are satisfied.

The stress function (A31) gives stresses

$$\sigma_{rr} = (\alpha-\beta^2)r^{\alpha-2}\cos\beta\theta \ , \tag{A33a}$$

$$\sigma_{\theta\theta} = \alpha(\alpha - 1)r^{\alpha-2}\cos\beta\theta \tag{A33b}$$

and

$$\sigma_{r\theta} = \beta(\alpha - 1)r^{\alpha-2}\sin\beta\theta \ . \tag{A33c}$$

These stresses, via equations (A29), give strains

$$2G\epsilon_{rr} = ((1 - s)(\alpha - \beta^2) - s\alpha(\alpha - 1))r^{\alpha-2}\cos\beta\theta \ , \tag{A34a}$$

$$2G\epsilon_{\theta\theta} = ((1 - s)\alpha(\alpha - 1) - s(\alpha - \beta^2))r^{\alpha-2}\cos\beta\theta \tag{A34b}$$

and

$$2G\epsilon_{r\theta} = (2\beta(\alpha - 1))r^{\alpha-2}\sin\beta\theta \ . \tag{A34c}$$

For simplicity in later calculations, the functions

$$A = ((1 - s)(\alpha - \beta^2) - s\alpha(\alpha - 1)) \ , \tag{A34d}$$

$$B = ((1 - s)\alpha(\alpha - 1) - s(\alpha - \beta^2)) \tag{A34e}$$

and

$$C = (2\beta(\alpha - 1)) \tag{A34f}$$

are defined.

In terms of these functions, the strain-displacement equation (A30a) becomes

$$\partial/\partial r \ (2Gu_r) = Ar^{\alpha-2}\cos\beta\theta \ , \tag{A35a}$$

which integrates to

$$2Gu_r = ((A/(\alpha - 1))r^{\alpha-1}\cos\beta\theta + h'(\theta) \quad . \tag{A35b}$$

Using (A35b) and (A34b) in the strain-displacement equation (A30b) and integrating gives

$$2Gv_\theta = (1/\beta)((B - (A/(\alpha - 1))r^{\alpha-1}\sin\beta\theta - h(\theta) + g(r) \ , \tag{A36}$$

so that equation (A30c) can be reduced to

$$h''(\theta)/r + h(\theta)/r + r^{-1}(\partial/\partial r(g(r)/r)) = D \ , \tag{A37a}$$

where

$$D = (C + \beta A/(\alpha - 1) - ((\alpha - 2)/\beta)(B - (A/(\alpha - 1)))) \ . \tag{A37b}$$

The result of using relations (A32a,b) to evaluate the coefficients in equations (A35b), (A36), and (A37) is shown in Table 15.

Table 15. Displacement Derivation Symmetric Coefficient Values.

Coefficients	$\alpha = \beta$	$\alpha - 2 = \beta$
$A/(\alpha - 1)$	$-\alpha$	$4 - \alpha - 4s$
$(1/\beta)(B - A/(\alpha - 1))$	α	$2 + \alpha - 4s$
D	0	0

Since $D = 0$ for the admissible values of α and β, equation (A37a) becomes

$$h''(\theta) + h(\theta) + r^2(\partial/\partial r(g(r)/r)) = 0 \quad , \tag{A38}$$

which can be separated into

$$h''(\theta) + h(\theta) = M \tag{A39a}$$

and

$$r^2(\partial/\partial r(g(r)/r)) = -M \tag{A39b}$$

where M is the separation constant. The solutions to (A39), using integration constants F, H and K, are

$$h(\theta) = M + K\sin(\theta) - H\cos(\theta) \tag{A40a}$$

and

$$g(r) = M + Fr \quad . \tag{A40b}$$

The contributions of equations (A40) to the displacements are:

$$\text{to } u_r; \quad h'(\theta) = K\cos(\theta) + H\sin(\theta) \quad , \tag{A41a}$$

$$\text{to } v_\theta; \quad -h(\theta) + g(r) = -K\sin(\theta) + H\cos(\theta) + Fr \quad , \tag{A41b}$$

so that the separation constant M is of no consequence. Equations (A41) are, of course, the rigid-body displacement terms.

In the derivation of the antisymmetric displacement components the rigid body terms are ignored since they have been determined.

The antisymmetric part of the stress function has the form

$$\Phi_{an}(r,\theta) = r^{\alpha}\sin\beta\theta \ , \tag{A42}$$

and (A32) holds as before. The corresponding stresses are

$$\sigma_{rr} = (\alpha - \beta^2)r^{\alpha-2}\sin\beta\theta \ , \tag{A43a}$$

$$\sigma_{\theta\theta} = \alpha(\alpha - 1)r^{\alpha-2}\sin\beta\theta \tag{A43b}$$

and

$$\sigma_{r\theta} = -\beta(\alpha - 1)r^{\alpha-2}\cos\beta\theta \ . \tag{A43c}$$

The coefficient in the $\sigma_{r\theta}$ equation is the negative of that in the corresponding symmetric equation (A33c). The antisymmetric strains are

$$2G\epsilon_{rr} = Ar^{\alpha-2}\sin\beta\theta \ , \tag{A44a}$$

$$2G\epsilon_{\theta\theta} = Br^{\alpha-2}\sin\beta\theta \tag{A44b}$$

and

$$2G\epsilon_{r\theta} = -Cr^{\alpha-2}\cos\beta\theta \ . \tag{A44c}$$

Proceeding as for the symmetric part, integration of the strain-displacement equations gives

$$2Gu_r = (A/(\alpha - 1))r^{\alpha-1}\sin\beta\theta \tag{A45a}$$

and

$$2Gv_\theta = (1/\beta)(A/(\alpha - 1) - B)r^{\alpha-1}\cos\beta\theta \ . \tag{A45b}$$

Evaluation of the shear strain-displacement equation (A30c) gives, as a computational check, the right hand side

$$(C + \beta A/(\alpha - 1) + ((\alpha - 2)/\beta)(A/(\alpha - 1) - B)) \quad , \qquad (A46)$$

which is identical to D (equation (A37b)).

The result of using (A32a,b) to evaluate the coefficients in equations (A45) and (A46) is shown in Table 16.

Table 16. Displacement Derivation Antisymmetric Coefficient Values.

Coefficients	$\alpha = \beta$	$\alpha - 2 = \beta$
$A/(\alpha - 1)$	$-\alpha$	$4 - \alpha - 4s$
$(1/\beta)(A/(\alpha - 1) - B)$	$-\alpha$	$4s - \alpha - 2$
(A46)	0	0

The coefficients in Table 15, along with equation (A27a), when substituted into equations (A35b) and (A36) lead to the symmetric displacement eigenfunctions,

$$(2Gu_r)_s = \hat{C}_{ns} r^{n/2}[-(n/2 + 1)\sin(n/2 = 1)\theta$$

$$- ((n/2 + 1)/(n/2 + (-1)^n))(3 - 4s - n/2)\sin(n/2 - 1)\theta] \quad (A47a)$$

and

$$(2Gv_\theta)_s = \hat{C}_{ns} r^{n/2}[(n/2 + 1)\sin(n/2 + 1)\theta$$

$$- ((n/2 + 1)/(n/2 + (-1)^n))(3 - 4s + n/2)\sin(n/2 - 1)\theta], \quad (A47b)$$

while the coefficients in Table 16, with equation (A27b), substituted into (A45a,b), lead to the antisymmetric displacement eigenfunctions

$$(2Gu_r)_a = \hat{C}_{na} r^{n/2}[-(n/2 + 1)\sin(n/2 + 1)\theta$$

$$- ((n/2 + 1)/(n/2 - (-1)^n))(3 - 4s - n/2)\sin(n/2 - 1)\theta] \quad (A48a)$$

and

$$(2Gv_\theta)_a = \hat{C}_{na} r^{n/2}[-(n/2 + 1)\cos(n/2 + 1)\theta$$

$$- ((n/2 + 1)/(n/2 - (-1)^n))(-3 + 4s - n/2)\cos(n/2 - 1)\theta]. \quad (A48b)$$

Special Eigenvalues

The special values of λ previously noted, and the corresponding eigenvalues n are shown in Table 17.

Table 17. Special Eigenvalues.

λ	n
-1	-2
0	0
+1	+2

Physically, the displacements are necessarily everywhere bounded and continuous except at the crack faces. It is immediately

apparent that all negative eigenvalues must be discarded.

The eigenvalue n=0 corresponds to the stress function

$$\Phi_o(r,\theta) = rf_o(\theta) \tag{A49}$$

which, when substituted into equation (A2), gives the ordinary differential equation

$$(D_\theta^2 + 1)^2 f_o(\theta) = 0 \quad , \tag{A50}$$

with solution

$$f_o(\theta) = K_1\sin\theta + K_2\cos\theta + K_3\theta\sin\theta + K_4\theta\cos\theta \quad . \tag{A51}$$

The corresponding stresses are

$$\sigma_{rro} = (2/r)\,(K_3\cos\theta - K_4\sin\theta) \quad , \tag{A52a}$$

$$\sigma_{\theta\theta o} = 0 \tag{A52b}$$

and

$$\sigma_{r\theta o} = 0 \quad . \tag{A52c}$$

The crack face boundary conditions are identically satisfied. Calculation of the displacements yields

$$(2Gu_r)_o = 2(1 - s)\ln(r)(K_3\cos\theta - K_4\sin\theta) \tag{A53a}$$

and

$$(2Gv_\theta)_o = -2(s + (1 - s)\ln(r))(K_3\sin\theta - K_4\cos\theta) \quad , \tag{A53b}$$

so that bounded displacements require that the zero eigenvalue be discarded.

The remaining special eigenvalue is n=2. The corresponding stress function is

$$\Phi_2(r,\theta) = r^2 f_2(\theta) \quad , \tag{A54}$$

which satisfies the biharmonic equation if

$$D_\theta^2(D_\theta^2 + 4)f_2(\theta) = 0 \quad ; \tag{A55a}$$

that is, for

$$f_2(\theta) = K_1 + K_2\theta + K_3 \sin 2\theta + K_4 \cos 2\theta \quad . \tag{A55b}$$

Calculation of stresses, substitution into the stress-strain equations and application of the crack face boundary conditions requires

$$K_2 = 0 \ ,$$

$$K_3 = 0 \tag{A56}$$

and

$$K_1 + K_4 = 0 \ ,$$

so that

$$\Phi_2(r,\theta) = K_4 r^2(\cos 2\theta - 1) \quad . \tag{A57}$$

The general solution eigenfunctions for n = 2 are

$$C_{2s} r^2(\cos 2\theta - 1)$$

and

$$\mathcal{C}_{2a} r^2 \sin 2\theta \ . \tag{A58b}$$

Clearly, the general solution n = 2 antisymmetric term must be discarded. Physically, this term corresponds to a state of uniform shear, which obviously cannot be supported with stress free crack faces.

Stress and Displacement Fields

A two-dimensional displacement field which satisfies free-crack-face boundary conditions can now be written as

$$2Gu_r = K\cos\theta + H\sin\theta \tag{A59}$$

$$+ \sum_{n=1}^{\infty} \mathcal{C}_{ns} r^{n/2} [-(n/2 + 1)\cos(n/2 + 1)\theta$$

$$- ((n/2 + 1)/(n\ 2 + (-1)^n))(3 - 4s - n/2)\cos(n/2 - 1)\theta]$$

$$+ \sum_{\substack{n=1 \\ n\neq 2}}^{\infty} \mathcal{C}_{na} r^{n/2} [-(n/2 + 1)\sin(n/2 + 1)\theta$$

$$- ((n/2 + 1)/(n/2 - (-1)^n))(3 - 4s - n/2)\sin(n/2 - 1)\theta]$$

and

$$2Gv_\theta = Fr - K\sin\theta + H\cos\theta \tag{A60}$$

$$+ \sum_{n=1}^{\infty} \mathcal{C}_{ns} r^{n/2} [(n/2 + 1)\sin(n/2 + 1)\theta$$

$$- ((n/2 + 1)/(n/2 + (-1)^n))(3 - 4s + n/2)\sin(n/2 - 1)\theta]$$

$$+ \sum_{\substack{n=1 \\ n\neq 2}}^{\infty} \hat{C}_{na} r^{n/2}[-(n/2 + 1)\cos(n/2 + 1)\theta$$

$$- ((n/2 + 1)/(n/2 - (-1)^n))(-3 + 4s - n/2)\cos(n/2 - 1)\theta] .$$

It is convenient, for numerical calculation, to nodimensionalize the displacements and to separate the displacement equations into parts dependent upon, and independent of, the material property (Poisson's ratio) parameter. So doing, equation (A59) becomes

Table 18. Nondimensionalized Coefficients

$\bar{C}_{ns}$	$= (C_{ns}L^{(n/2 - 1)})/4G$
$\bar{C}_{na}$	$= (C_{na}L^{(n/2 - 1)})/4G$
$\bar{u}_r$	$= u_r/L$
$\bar{v}_\theta$	$= v_\theta/L$
$\bar{H}$	$= H/2GL$
$\bar{K}$	$= K/2GL$
$\bar{F}$	$= F/2G$
$\bar{r}$	$= r/L$

$$\bar{u}_r = \bar{K}\cos\theta + \bar{H}\sin\theta \qquad \text{(A61a)}$$

$$+ \sum_{n=1}^{\infty} \bar{C}_{ns}\bar{r}^{n/2}[-(n+2)\cos(n/2+1)\theta$$

$$- ((n+2)/(n+2(-1)^n))(6-n)\cos(n/2-1)\theta$$

$$+ 8s((n+2)/(n+2(-1)^n))\cos(n/2-1)\theta]$$

$$+ \sum_{\substack{n=1 \\ n\neq 2}}^{\infty} \bar{C}_{na}\bar{r}^{n/2}[-(n+2)\sin(n/2+1)\theta$$

$$- ((n+2)/(n-2(-1)^n))(6-n)\sin(n/2-1)\theta$$

$$+ 8s((n+2)/(n-2(-1)^n))\sin(n/2-1)\theta] \ ,$$

while (A60) becomes

$$\bar{v}_\theta = \bar{F}\bar{r} - \bar{K}\sin\theta + \bar{H}\cos\theta \qquad \text{(A62a)}$$

$$+ \sum_{n=1}^{\infty} \bar{C}_{ns}\bar{r}^{n/2}[(n+2)\sin(n/2+1)\theta$$

$$- ((n+2)/(n+2(-1)^n))(6+n)\sin(n/2-1)\theta$$

$$+ 8s((n+2)/(n+2(-1)^n))\sin(n/2-1)\theta]$$

$$+ \sum_{\substack{n=1 \\ n\neq 2}}^{\infty} \bar{C}_{na}\bar{r}^{n/2}[-(n+2)\cos(n/2+1)\theta$$

$$+ ((n + 2)/(n - 2(-1)^n))(6 + n)\cos(n/2 - 1)\theta$$

$$- 8s((n + 2)/(n - 2(-1)^n))\cos(n/2 - 1)\theta] .$$

In these equations the symbols of Table 18 are used along with the characteristic length L defined in Chapter II.

Using the notation

$$\bar{u}_{ns} = \bar{r}^{n/2}[-(n + 2)\cos(n/2 + 1)\theta$$

$$- ((n + 2)/(n + 2(-1)^n))(6 - n)\cos(n/2 - 1)\theta] ,$$

$$\bar{v}_{ns} = \bar{r}^{n/2}[(n + 2)\sin(n/2 + 1)\theta$$

$$- ((n + 2)/(n + 2(-1)^n))(6 + n)\sin(n/2 - 1)\theta] ,$$

$$\hat{u}_{ns} = 8\bar{r}^{n/2}((n + 2)/(n + 2(-1)^n))\cos(n/2 - 1)\theta ,$$

$$\hat{v}_{ns} = 8\bar{r}^{n/2}((n + 2)/(n + 2(-1)^n))\sin(n/2 - 1)\theta ,$$

$$\bar{u}_{na} = \bar{r}^{n/2}[- (n + 2)\sin(n/2 + 1)\theta$$

$$- ((n + 2)/(n - 2(-1)^n))(6 - n)\sin(n/2 + 1)\theta] ,$$

$$\bar{v}_{na} = \bar{r}^{n/2}[- (n + 2)\cos(n/2 + 1)\theta$$

$$+ ((n + 2)/(n - 2(-1)^n))(6 + n)\cos(n/2 - 1)\theta] ,$$

$$\hat{u}_{na} = 8\bar{r}^{n/2}((n + 2)/(n - 2(-1)^n))\sin(n/2 - 1)\theta$$

and

$$\hat{v}_{na} = 8\bar{r}^{n/2}(- (n + 2)/(n - 2(-1)^n))\cos(n/2 - 1)\theta ,$$

equations (A61) and (A62) may be written as

$$\bar{u}_r = \bar{K}\cos\theta + \bar{H}\sin\theta$$

$$+ \sum_{n=1}^{\infty} \bar{C}_{ns}(\bar{u}_{ns} + s\hat{u}_{ns}) + \sum_{\substack{n=1 \\ n\neq 2}}^{\infty} \bar{C}_{na}(\bar{u}_{na} + s\hat{u}_{na})$$

and

$$\bar{v}_\theta = \bar{F}\bar{r} - \bar{K}\sin\theta + \bar{H}\cos\theta$$

$$+ \sum_{n=1}^{\infty} \bar{C}_{ns}(\bar{v}_{ns} + s\hat{v}_{ns}) + \sum_{\substack{n=1 \\ n\neq 2}}^{\infty} \bar{C}_{na}(\bar{v}_{na} + s\hat{v}_{na}) \quad .$$

For completeness, the stress eigenfunctions, nondimensionalized with respect to the shear modulus ($\bar{\sigma} = \sigma/G$) are, from (A8), (A25) and (A26),

$$\bar{\sigma}_{rr} = \sum_{n=1}^{\infty} \bar{C}_{ns}\bar{r}^{(n/2 - 1)}(n)(n + 2)[-\cos(n/2 + 1)\theta \qquad \text{(A63)}$$

$$+ ((n - 6)/(n + 2(-1)^n))\cos(n/2 - 1)\theta]$$

$$+ \sum_{\substack{n=1 \\ n\neq 2}}^{\infty} \bar{C}_{na}\bar{r}^{(n/2 - 1)}(n)(n + 2)[-\sin(n/2 + 1)\theta$$

$$+ ((n - 6)/(n - 2(-1)^n))\sin(n/2 - 1)\theta] \quad ,$$

$$\bar{\sigma}_{\theta\theta} = \sum_{n=1}^{\infty} \bar{C}_{ns}\bar{r}^{(n/2 - 1)}(n)(n + 2)[\cos(n/2 + 1)\theta \tag{A64}$$

$$- ((n + 2)/(n + 2(-1)^n))\cos(n/2 - 1)\theta]$$

$$+ \sum_{\substack{n=1 \\ n\neq 2}}^{\infty} \bar{C}_{na}\bar{r}^{(n/2 - 1)}(n)(n + 2)[\sin(n/2 + 1)\theta$$

$$- ((n + 2)/(n - 2(-1)^n))\sin(n/2 - 1)\theta]$$

and

$$\bar{\sigma}_{r\theta} = \sum_{n=1}^{\infty} \bar{C}_{ns}\bar{r}^{(n/2 - 1)}(n)(n + 2)[\sin(n/2 + 1)\theta \tag{A65}$$

$$- ((n - 2)/(n + 2(-1)^n))\sin(n/2 - 1)\theta]$$

$$+ \sum_{\substack{n=1 \\ n\neq 2}}^{\infty} \bar{C}_{na}\bar{r}^{(n/2 - 1)}(n)(n + 2)[- \cos(n/2 + 1)\theta$$

$$+ ((n - 2)/(n - 2(-1)^n))\cos(n/2 - 1)\theta] \quad .$$

Stress Intensity Factors

The stress intensity factors K_I and K_{II} are defined in terms of the near-tip stress by

$$K_I = \lim_{r\to 0} (2\pi r)^{\frac{1}{2}} \sigma_{\theta\theta}(r,0) \tag{A66a}$$

and

$$K_{II} = \lim_{r \to 0} (2\pi r)^{\frac{1}{2}} \sigma_{r\theta}(r,0) \tag{A67a}$$

The nondimensionalization of r and σ requires the modification of these equations to

$$K_I = \lim_{\bar{r} \to 0} (2\pi L\bar{r})^{\frac{1}{2}} G\bar{\sigma}_{\theta\theta}(\bar{r},0) \tag{A66b}$$

and

$$K_{II} = \lim_{\bar{r} \to 0} (2\pi L\bar{r})^{\frac{1}{2}} G\bar{\sigma}_{r\theta}(\bar{r},0) \quad . \tag{A67b}$$

Use of $\bar{\sigma}_{\theta\theta}$ from (A64), and of $\bar{\sigma}_{r\theta}$ from (A65) gives

$$K_I = 12G(2\pi L)^{\frac{1}{2}} \bar{C}_{1s} \tag{A66c}$$

and

$$K_{II} = -\ 4G(2\pi L)^{\frac{1}{2}} \bar{C}_{1a} \quad . \tag{A67c}$$

APPENDIX B

FINITE ELEMENT EQUATIONS FOR LINEAR ELASTODYNAMIC SYSTEMS

In this appendix, the linear elasticity equations of motion are developed in matrix form. These equations are then specialized to the high-order singularity element, and the relationship between the Williams' eigenfunctions and the element stiffness, consistent mass, and consistent force matrices is shown. In Zienkiewicz [1] terminology, the "generalized coordinate" method is used, with the Williams' coefficients (Appendix A) as the generalized coordinates. This formulation is particularly appropriate here, since the coefficients $\bar{C}_{1s}$ and $\bar{C}_{1a}$ are directly proportional to the stress intensity factors K_I and K_{II}.

General Equations

As is well known [1-3] the governing equations of linear elasticity may be written in matrix form by arranging the stress and strain tensors as vectors, and Hooke's tensor as a square matrix. Using this artifice, the strain displacement relations become

$$\underline{\varepsilon} = \underset{\sim}{D}\, \underline{u} \ , \tag{B1}$$

while the constitutive relation (Hooke's law) is

$$\underline{\sigma} = \underset{\sim}{H}\, \underline{\varepsilon} \ , \tag{B2}$$

and the arrangement of the various matrices depends on the exact

formulation sought [2].

Hamilton's Principle

Hamilton's principle [58] may be mathematically stated as

$$\delta A = 0 \ , \tag{B3a}$$

where δ is the variational operator [59] and

$$A = \int_{t_1}^{t_2} L dt \tag{B3b}$$

is the action functional and the Lagrangian

$$L = T - U - W_p \tag{B3c}$$

is formed from

Kinetic energy; $$T = \tfrac{1}{2} \int_V \rho \, \dot{\underline{u}}^T \dot{\underline{u}} \, dV \ , \tag{B4a}$$

Potential energy; $$U = \tfrac{1}{2} \int_V \underline{\varepsilon}^T \underline{\sigma} \, dV \tag{B4b}$$

and

External Force Potential; $$W_p = - \int_V \underline{u}^T \underline{X} \, dV - \int_{S_1} \underline{u}^T \underline{T} \, dS \ . \tag{B4c}$$

Here, $\underline{X}$ is the body force vector and $\underline{T}$ is the surface traction vector specified on the portion of the boundary S_1.

Using (B4) and (B3c) in (B3a), the action functional is

$$A = \int_{t_1}^{t_2} \left[\tfrac{1}{2} \int_V (\dot{\underline{u}}^T \dot{\underline{u}} \rho - \underline{\varepsilon}^T \underline{\sigma} + 2\underline{u}^T \underline{X}) dV + \int_{S_1} \underline{u}^T \underline{T} \, dS \right] dt \quad . \tag{B5a}$$

In applying Hamilton's principle, it is necessary to write (B5a) in terms of displacements by use of the constitutive and strain-displacement relations. The result is

$$A = \int_{t_1}^{t_2} \left[\tfrac{1}{2} \int_V (\rho \dot{\underline{u}}^T \dot{\underline{u}} - \underline{u}^T \underset{\sim}{D}^T \underset{\sim}{\underset{\sim}{H}} \underset{\sim}{D} \underline{u} + 2u^T X) dV + \int_{S_1} \underline{u}^T \underline{T} \, dS \right] dt \quad . \tag{B5b}$$

The first variation of (B5b) is

$$\delta A = \int_{t_1}^{t_2} \left[\int_V \rho \underline{\delta \dot{u}}^T \dot{\underline{u}} - \underline{\delta u}^T \underset{\sim}{D}^T \underset{\sim}{H} \underset{\sim}{D} \underline{u} + \underline{\delta u}^T \underline{X} \, dV + \int_{S_1} \underline{\delta u}^T \underline{T} \, dS \right] dt \tag{B6a}$$

and must be equal to zero. Since

$$\underline{\delta \dot{u}}^T \dot{\underline{u}} = (\partial/\partial t(\underline{\delta u}^T \dot{\underline{u}} - \underline{\delta u}^T \ddot{\underline{u}})) \quad , \tag{B7a}$$

the first term in (B6a) may be written

$$\int_{t_1}^{t_2} \int_V \rho \, \underline{\delta \dot{u}}^T \dot{\underline{u}} \, dV \, dt = - \int_{t_1}^{t_2} \int_V \rho \, \underline{\delta u}^T \ddot{\underline{u}} \, dV \, dt$$

$$+ \int_{t_1}^{t_2} \int_V \rho (d/dt(\underline{\delta u}^T \dot{\underline{u}})) dV \, dt \quad , \tag{B7b}$$

and the last term in (B7b) transformed from

$$\int_{t_1}^{t_2} \int_V \rho(d/dt(\underline{\delta u}^T \underline{\dot{u}}))dV\ dt \qquad \text{(B7c)}$$

to

$$\int_{t_1}^{t_2} (d/dt) \int_V \rho \underline{\delta u}^T \underline{\dot{u}}\ dV))dt \qquad \text{(B7d)}$$

and finally to

$$\left[\int_V \rho\ \underline{\delta u}^T \underline{\dot{u}}\ dV\right]_{t_2}^{t_1} = 0\ , \qquad \text{(B7e)}$$

where the first transformation holds because the region of interest V contains the same material at all times and the integrated term is zero since the displacement variations $\underline{\delta u}$ vanish at the ends of the time interval.

The result (B7e) reduces (B6a) to

$$\int_{t_1}^{t_2} \left[\int_V \underline{\delta u}^T(\rho\underline{\ddot{u}} + \underset{\sim}{D}^T \underset{\sim}{H}\ \underset{\sim}{D}\ \underline{u} - \underline{X})\ dV - \int_{S_1} \underline{\delta u}^T \underline{T}\ dS\right] dt = 0\ , \qquad \text{(B6b)}$$

which is a form suitable for generation of the finite element equations of motion.

Element Displacement Field

The displacement field in an element can be approximated in terms of a chosen set of functions $\underline{f}$ and the corresponding generalized

coordinates $\underline{C}$, by

$$\underline{u} = \underset{\sim}{f}\,\underline{C} \ , \tag{B8a}$$

where, for an n node element in plane elasticity,

$\underline{u}$ is the (2 x 1) displacement vector,

$\underset{\sim}{f}$ is the (2 x 2n) matrix of coordinate functions, and

$\underline{C}$ is the (2n x 1) vector of generalized coordinates.

In the present formulation, the element geometry is most easily described in cartesian coordinates, while the coordinate functions are expressed in polar coordinates. It is therefore necessary to modify (B8a) to

$$\underline{u} = \underset{\sim}{R}\,\underset{\sim}{f}\,\underline{C} \tag{B8b}$$

where now $\underline{u}$ is a cartesian displacement vector, and $\underset{\sim}{R}$ is the appropriate (2 x 2) rotation matrix.

The element displacement field can be related to the element's nodal displacements by evaluating (B8b) at the nodal points, thus generating

$$\hat{\underline{u}} = \underset{\sim}{A}\,\underline{C} \ , \tag{B9a}$$

where

$\hat{\underline{u}}$ is the (2n x 1) nodal point displacement vector, and

$\underset{\sim}{A}$ is a (2n x 2n) transformation matrix.

For reasonable element topology (B9a) can be inverted to obtain the generalized coordinates in terms of the nodal point displacements

$$\underline{C} = \underset{\sim}{A}^{-1}\hat{\underline{u}} \quad . \tag{B9b}$$

Equation (B9b) substituted into (B8b) gives the expression for the element displacement field as

$$\underline{u} = \underset{\sim}{R}\,\underset{\sim}{f}\,\underset{\sim}{A}^{-1}\hat{\underline{u}} \ , \tag{B10a}$$

or, defining

$$\underset{\sim}{N} = \underset{\sim}{R}\,\underset{\sim}{f}\,\underset{\sim}{A}^{-1} \quad , \tag{B10b}$$

as

$$\underline{u} = \underset{\sim}{N}\,\hat{\underline{u}} \quad . \tag{B10c}$$

The $\underset{\sim}{N}$ are called in [1] "shape functions" and need not be derived from generalized coordinates.

Element Equations of Motion

Proceeding with development of the finite element equations of motion, (B10c) substituted into (B6b) gives

$$\int_{t_1}^{t_2}\left[\int_V \hat{\underline{\delta u}}^T\left(\rho\,\underset{\sim}{N}^T\underset{\sim}{N}\ddot{\hat{\underline{u}}} + \underset{\sim}{N}^T\underset{\sim}{D}^T\underset{\sim}{H}\,\underset{\sim}{D}\,\underset{\sim}{N}\hat{\underline{u}} - \underset{\sim}{N}^T\underline{X}\right) dV - \int_{S_1}\hat{\underline{\delta u}}^T\underset{\sim}{N}^T\underline{T}\,dS\right] dt = 0, \tag{B6c}$$

in which the time-independence of $\underset{\sim}{N}$ has been used. Since the nodal displacements are independent of the volume and surface integrals, (B6c) may be rewritten as

$$\int_{t_1}^{t_2}\hat{\underline{\delta u}}^T\left[\int_V \rho\underset{\sim}{N}^T\underset{\sim}{N}\,dV\,\ddot{\hat{\underline{u}}} + \int_V \underset{\sim}{N}^T\underset{\sim}{D}^T\underset{\sim}{H}\,\underset{\sim}{D}\,\underset{\sim}{N}\,dV\,\hat{\underline{u}} - \int_V \underset{\sim}{N}^T\underset{\sim}{X}\,dV\right.$$

$$- \int_{S_1} \underset{\sim}{N}^T \underline{T} \, dS \Big] \, dt = 0 \quad , \tag{B6d}$$

from which the usual argument on independence of the displacement variations leads to the equations of motion

$$\underset{\sim}{M} \, \underline{\ddot{\hat{u}}} + \underset{\sim}{K} \, \underline{\hat{u}} = \underline{F}_b + \underline{F}_s \quad , \tag{B11}$$

where

$$\underset{\sim}{M} = \int_V \rho \underset{\sim}{N}^T \underset{\sim}{N} \, dV \quad , \tag{B12a}$$

$$\underset{\sim}{K} = \int_V \underset{\sim}{N}^T \underset{\sim}{D}^T \underset{\sim}{H} \, \underset{\sim}{D} \, \underset{\sim}{N} \, dV \quad , \tag{B13a}$$

$$\underline{F}_b = \int_V \underset{\sim}{N}^T \underline{X} \, dV \tag{B14a}$$

and

$$\underline{F}_s = \int_{S_1} \underset{\sim}{N}^T \underline{T} \, dS \quad . \tag{B15a}$$

This formulation is, of course, perfectly general within the framework of linear elasticity.

Singularity Element Matrices

For the high-order singularity elements used in this investigation, the relevant consistent mass matrix becomes

$$\underset{\sim}{M} = \int_V \rho \, \underset{\sim}{A}^{-T} \underset{\sim}{f}^T \underset{\sim}{R}^T \underset{\sim}{R} \, \underset{\sim}{f} \, \underset{\sim}{A}^{-1} \, dV \tag{B12b}$$

or

$$\underset{\sim}{M} = \underset{\sim}{A}^{-T} \int_V \rho \underset{\sim}{f}^T \underset{\sim}{f} \, dV \, \underset{\sim}{A}^{-1} \quad , \tag{B12c}$$

where the orthogonality of the $\underset{\sim}{R}$ matrix was used.

This last expression for the consistent mass matrix can be written as

$$\underset{\sim}{M} = \underset{\sim}{A}^{-T} \underset{\sim}{M}_c \, \underset{\sim}{A}^{-1} \quad , \tag{B12d}$$

where

$$\underset{\sim}{M}_c = \int_V \rho \underset{\sim}{f}^T \underset{\sim}{f} \, dV \tag{B12e}$$

is known as the "consistent mass matrix with respect to the generalized coordinates." A similar rearrangement for (B13a-B15a) yields

$$\underset{\sim}{K} = \underset{\sim}{A}^{-T} \underset{\sim}{K}_c \underset{\sim}{A}^{-1} \quad , \tag{B13c}$$

$$\underset{\sim}{K}_c = \int_V \underset{\sim}{f}^T \underset{\sim}{R}^T \underset{\sim}{D}^T \underset{\sim}{H} \, \underset{\sim}{D} \, \underset{\sim}{R} \, \underset{\sim}{f} \, dV \tag{B13d}$$

and

$$\underline{F} = \underset{\sim}{A}^{-T} (\underline{F}_{bc} + \underline{F}_{sc}) \quad , \tag{B15b}$$

$$\underline{F}_{bc} = \int_V \underset{\sim}{f}^T \underset{\sim}{R}^T \underline{X} \, dv \quad , \tag{B15c}$$

$$\underline{F}_{sc} = \int_{S_1} \underset{\sim}{f}^T \underset{\sim}{R}^T \underline{T} \, dS \quad . \tag{B15d}$$

Finally, when the dependence of the $\underset{\sim}{f}$ matrix on the Poisson's ratio parameter s is made explicit,

$$\underset{\sim}{f} = \underset{\sim}{f}_1 + s\underset{\sim}{f}_2 \ , \tag{B16a}$$

so that

$$\underset{\sim}{A} = \underset{\sim}{A}_1 + s\underset{\sim}{A}_2 \ . \tag{B16b}$$

Substitution of (B16a) into (B12e) gives

$$\underset{\sim}{M}_c = \hat{\underset{\sim}{M}}_{c11} + s\hat{\underset{\sim}{M}}_{c12} + \hat{s}\hat{\underset{\sim}{M}}_{c22} \tag{B17a}$$

where

$$\hat{\underset{\sim}{M}}_{c11} = \int_V \rho \underset{\sim}{f}_1^T \underset{\sim}{f}_1 \, dV \ , \tag{B17b}$$

$$\hat{\underset{\sim}{M}}_{c12} = \int_V \rho(\underset{\sim}{f}_1^T \underset{\sim}{f}_2 + \underset{\sim}{f}_2^T \underset{\sim}{f}_1) \, dV \tag{B17c}$$

and

$$\hat{\underset{\sim}{M}}_{c22} = \int_V \rho \underset{\sim}{f}^T \underset{\sim}{f}_2 \, dV \ . \tag{B17d}$$

APPENDIX C

THE TIME INTEGRATION ALGORITHM

In this appendix, the reasons for choice of the constant-average-acceleration variant of the Newmark-β time integration algorithm are given, and the particular equations implemented in the computer program are derived.

Operators Considered

The time integration operators considered for use in solving the equation

$$\underset{\sim}{M}\,\ddot{\underline{u}} + \underset{\sim}{K}\,\underline{u} = \underline{F} \tag{C1}$$

were:

1. The "Precise Integration Operator" [60];
2. The Wilson averaging operator [61];
3. The Gurtin averaging operator [62,63];
4. The modified central difference operator [29]; and
5. The "Newmark-β" operator [36-38].

The first four operators were unsuitable for these reasons:

1. The "Precise Integration Operator", as its name implies, is precise. In fact, it has neither spurious (algorithm induced) damping nor period error. Unfortunately, it requires modal decomposition (solution of the frequency eigenvalue problem) of the entire structure, so that its use is prohibitively expensive for even moderately

large systems.

2. Both the Wilson and Gurtin averaging operators have severe spurious damping, which requires short time steps if accurate higher mode response is to be maintained [60,64,65].

3. The modified central difference scheme is attractive in its ease of coding and computational economy, being little more complicated than matrix multiplication. It was unsuitable for this investigation, however, since it requires a lumped (diagonalized) mass matrix.

The Newmark-β method, then, remained. Its constant-average-acceleration ($\beta = \frac{1}{4}$) variant provided:

1. Numerical stability for any time-step size;
2. Absence of spurious damping;
3. Small and easily controlled phase error;
4. Modest computer core requirements; and
5. Ease of coding.

The first four characteristics are discussed at length, with numerical and graphical comparisons, in [60,64,65]. The fifth is evident in that the FORTRAN subroutine written to implement the algorithm, including special purpose sections peculiar to this investigation, required fewer than 250 statements.

The Algorithm

The algorithm used, a simplification of that developed in [38], is based on the relations proposed by Newmark in [36,37]; i.e.

$$\underline{\dot{u}}_{n+1} - \underline{\dot{u}}_n = h(1 - \gamma)\, \underline{\ddot{u}}_n + h\gamma\, \underline{\ddot{u}}_{n+1} \qquad \text{(C2a)}$$

and

$$\underline{u}_{n+1} - \underline{u}_n = h\,\dot{\underline{u}}_n + h^2(\tfrac{1}{2} - \beta)\,\ddot{\underline{u}}_n + \beta h^2\,\ddot{\underline{u}}_{n+1}\,, \qquad (C2b)$$

where

$(\dot{\ }) = d/dt$

$h = \Delta t$, the time step, and

$\underline{u}_n$ is the displacement vector at $t-t_o = nh$.

Newmark proved that, unless $\gamma = \frac{1}{2}$, there is spurious damping, while Nickell [64] showed $\beta = \frac{1}{4}$ to be optimum for numerical stability. With these values of the parameters, equations (C2) become

$$\dot{\underline{u}}_{n+1} - \dot{\underline{u}}_n = h/2(\ddot{\underline{u}}_n + \ddot{\underline{u}}_{n+1}) \qquad (C3a)$$

and

$$\underline{u}_{n+1} - \underline{u}_n = h\,\dot{\underline{u}}_n + h^2/4\,(\ddot{\underline{u}}_n + \ddot{\underline{u}}_{n+1})\,. \qquad (C3b)$$

Equations (C3) amount to successive applications of the trapezoidal rule, since if (C3a) is substituted into

$$\underline{u}_{n+1} - \underline{u}_n = h/2\,(\dot{\underline{u}}_n + \dot{\underline{u}}_{n+1}) \qquad (C4)$$

and the result simplified, (C3b) is obtained.

The velocity-acceleration relation (C3a), left multiplied by the mass matrix, is

$$\underset{\sim}{M}\,(\dot{\underline{u}}_{n+1} - \dot{\underline{u}}_n) = h/2\,\underset{\sim}{M}\,(\ddot{\underline{u}}_n + \ddot{\underline{u}}_{n+1})\,. \qquad (C5)$$

Using the rearranged equation of motion

$$\underset{\sim}{M}\,\underline{\ddot{u}} = \underline{F} - \underset{\sim}{K}\,\underline{u} \ , \tag{C6}$$

written for times $t-t_o = nh$ and $t-t_o = (n+1)h$ to eliminate the accelerations in (C5) yields

$$\underset{\sim}{M}\,(\underline{\dot{u}}_{n+1} - \underline{\dot{u}}_n) = h/2\,(\underline{F}_n + \underline{F}_{n+1} - \underset{\sim}{K}\,(\underline{u}_n + \underline{u}_{n+1})) \ . \tag{C7}$$

The displacement-acceleration relation (C3b) written for $t-t_o = (n+1)h$ and subtracted from the same equation written for $t-t_o = (n+2)h$ gives

$$\underline{u}_{n+2} - 2\,\underline{u}_{n+1} + \underline{u}_n = h\,(\underline{\dot{u}}_{n+1} - \underline{\dot{u}}_n) + h^2/4\,(\underline{\ddot{u}}_{n+2} - \underline{\ddot{u}}_n) \ . \tag{C8}$$

Equation (C8), left multiplied by the mass matrix, with velocities eliminated by (C7) and accelerations eliminated by (C6) becomes

$$\begin{aligned}\underset{\sim}{M}\,(\underline{u}_{n+2} - 2\,\underline{u}_{n+1} + \underline{u}_n) = {} & h^2/2(\underline{F}_n + \underline{F}_{n+1} - \underset{\sim}{K}(\underline{u}_n + \underline{u}_{n+1})) \\ & + h^2/4(\underline{F}_{n+2} - \underline{F}_n - \underset{\sim}{K}(\underline{u}_{n+2} - \underline{u}_n)) \ ,\end{aligned} \tag{C9}$$

which, upon collection of terms in $\underline{u}_{n+2}$, $\underline{u}_{n+1}$, and $\underline{u}_n$, becomes the following difference equation used in the computer program.

$$\begin{aligned}(\underset{\sim}{M} + h^2/4\,\underset{\sim}{K})\underline{u}_{n+2} = {} & 2(\underset{\sim}{M} - h^2/4\,\underset{\sim}{K})\underline{u}_{n+1} - (\underset{\sim}{M} + h^2/4\,\underset{\sim}{K})\underline{u}_n \\ & + h^2/4(\underline{F}_n + 2\underline{F}_{n+1} + \underline{F}_{n+2}) \ .\end{aligned} \tag{C10}$$

Equation (C10) agrees with (5) in [38], when that equation is

specialized to $\underset{\sim}{C} = 0$ (no damping) and $\beta = \frac{1}{4}$.

The recurrence relation (C10) enables calculation of displacements at time $t-t_o = (n+2)h$, if the displacements at the two earlier times $t-t_o = (n+1)h$ and $t-t_o = nh$ are known. Since the usual initial conditions are given velocity and displacement fields at time t_o, the algorithm requires a special starting step.

The displacement-acceleration equation (C3b), written for $t-t_o = h$ and rearranged, is

$$\underline{u}_1 = \underline{u}_o + h\,\dot{\underline{u}}_o + h^2/4\,(\ddot{\underline{u}}_o + \ddot{\underline{u}}_1) \quad . \tag{C11}$$

This equation, left multiplied by the mass matrix, with the accelerations eliminated by (C6), becomes after collection of terms, the starting equation,

$$(\underset{\sim}{M} + h^2/4\,\underset{\sim}{K})\underline{u}_1 = (\underset{\sim}{M} - h^2/4\,\underset{\sim}{K})\underline{u}_o + h\,\underset{\sim}{M}\,\dot{\underline{u}}_o + h^2/4(\underline{F}_o + \underline{F}_1) \quad . \tag{C12}$$

This equation agrees with (7) in [38] when that equation is specialized to $\underset{\sim}{C} = 0$ and $\beta = \frac{1}{4}$.

Equations (C10) and (C12) are the equations used in this investigation for numerical solution of the equations of motion.

LITERATURE CITED

1. Zienkiewiez, O. C., The Finite Element Method in Engineering Science, Second Edition, McGraw-Hill, London, 1971.

2. Przemieniecki, J. S., Theory of Matrix Structural Analysis, McGraw-Hill, New York, 1968.

3. De Sai, C. S., and J. F. Abel, Introduction to the Finite Element Method - A Numerical Method for Engineering Analysis, Van Nostrand Reinhold Company, 1972.

4. Oden, J. T., Finite Elements of Nonlinear Continua, McGraw-Hill, New York, 1972.

5. Argyris, J. H., Energy Theorems and Structural Analysis, Butterworth Scientific Publications, London, 1960.

6. Turner, M. J., R. W. Clough, A. C. Martin, and L. J. Topp, "Stiffness and Deflection Analysis of Complex Structures", J. Aero. Sci., 23, 805-823, 1956.

7. Singhal, A. C., "775 Selected References on the Finite Element Method and Matrix Methods of Structural Analysis, Report S-12 Civil Engineering Department, Laval University, Quebec, January, 1969.

8. Watwood, V. B., Jr., "The Finite Element Method for Predictions of Crack Behavior," Nuclear Engineering and Design, II, 323-332, 1969.

9. Anderson, G. P., et al., "Use of Finite Element Computer Programs in Fracture Mechanics," Int. J. Fracture Mech., I, 63-76, 1971.

10. Kobayashi, A. S., et al., "A Numerical Procedure for Estimating The Stress Intensity Factor of a Crack in a Finite Plate." J. Basic Eng., 96, 681-684, 1964.

11. Chan, S. K., et al., "On the Finite Element Method in Linear Fracture Mechanics," Engineering Fracture Mechanics, 2, 1-17, 1970.

12. Kobayashi, A. S. et al., Application of the Method of Finite Element Analysis to Two-Dimensional Problems in Fracture Mechanics, Department of Mechanical Engineering, University of Washington, TR No. 5. (NR 064 478), October, 1968.

13. Griffith, A. A., "The Phenomenon of Rupture and Flow in Solids", Phil. Trans. Roy. Soc., A221, 163, 1920.

14. Williams, M. L., "Stress Singularities Resulting From Various Boundary Conditions in Angular Corners of Plates in Extension", Journal of Applied Mechanics, 74, 526-528, 1952.

15. _____, "On the Stress Distribution at the Base of a Stationary Crack," Journal of Applied Mechanics, 24, 109-114, 1957.

16. _____, "The Bending Stress Distribution at the Base of a Stationary Crack," Journal of Applied Mechanics, 83, 78-82, 1961.

17. Byskov, E., "The Calculation of Stress Intensity Factors using the Finite Element Method with Cracked Elements", Int. J. Fracture Mechanics, 6, 159-167, 1970.

18. Tracey, D. M., "Finite Elements for Determinations of Crack Tip Elastic Stress Intensity Factors", Engineering Fracture Mechanics, 3, 255-265, 1971.

19. Walsh, P. F., "The Computation of Stress Intensity Factors by a Special Finite Element Technique", Int. J. Solids and Structures, 7, 1333-1342, 1971.

20. Pian, T. H. H., et al., Elastic Crack Analysis by a Finite Element Hybrid Method, Massachusetts Institute of Technology, AFOSR Contract F44620-67-C-0019.

21. Wilson, W. K., Crack Tip Finite Elements for Plane Elasticity, Westinghouse Research Laboratories Scientific Paper 71-1E7-FMPWR-P2, 7 June 1971.

22. Anderson, J. M., J. A. Aberson, and R. H. Hardy, "A High-Order Cracked Finite Element". Presented at the 13th Annual Symposium on Fracture and Flaws, Albuquerque, New Mexico, 2 March 1973.

23. Anderson, J. M., and J. A. Aberson, Private Communication, 1972.

24. Hardy, R. H., "A High-Order Finite Element for Two-Dimensional Crack Problems", Ph.D. Dissertation, Georgia Institute of Technology, 1974.

25. DeArantes e Oliveira, E. R., "Theoretical Foundations of the Finite Element Method", Int. J. Solids and Structures, 4, 929-952, 1968.

26. Tong, Pin, and T. H. H. Pian, "On the Convergence of the Finite

Element Method for Problems with Singularity", Int. J. Solids and Structures, 9, 313-321, 1973.

27. Archer, J. S., "Consistent Mass Matrix for Distributed Mass Systems", Journal of the Structural Division, ASCE, 89, No. ST4, 161-178, 1963.

28. Tong, P, T. H. H. Pian and L. L. Bucciarelli, "Mode Shapes and Frequencies by Finite Elements Using Consistent and Lumped Masses", Int. J. Computers and Structures, 1, 623-638, 1971.

29. Key, S. W., and Z. E. Beisinger, The Transient Dynamic Analysis of Thin Shells by the Finite Element Method, SC-DC-713889.

30. Clough, R. W., "Analysis of Structural Vibrations and Dynamic Response", in Recent Advances in Matrix Methods of Structural Analysis and Design, Edited by R. H. Gallagher, Y. Yamada and J. T. Oden, University of Alabama Press, 1971.

31. Love, A. E. H., A Treatise on the Mathematical Theory of Elasticity, Dover, 1944.

32. Coker, E. G., and L. N. G. Filon, A Treatise on Photoelasticity, Cambridge, 1957.

33. Timoshenko, S. P., and J. N. Goodier, Theory of Elasticity, 3rd Edition, McGraw-Hill, 1970.

34. Anderson, J. M., Private Communication, 1972.

35. Malluck, J. F., Evaluation of the Dynamic Properties of a Special Finite Element for Fracture Mechanics, Unpublished Masters Degree report, Georgia Institute of Technology, 1973.

36. Newmark, N. M., Computation of Dynamic Structural Response in the Range Approaching Failure, Proceedings of the Symposium on Earthquake and Blast Effects on Structures, Los Angeles, 1952. Published by the Earthquake Engineering Research Institute.

37. Newmark, N. M., "A Method of Computation for Structural Dynamics", Journal of the Engineering Mechanics Division, ASCE, 85, No. EM3, 1959. Proc. Paper 2094.

38. Chan, S. P., H. L. Cox, and W. A. Benfield, "Transient Analysis of Forced Vibrations of Complex Structural-Mechanical Systems", Journal of the Royal Aeronautical Society, 66, 457-460, 1962.

39. Sih, G. C., and G. T. Embley, Mechanics of Impact and Crack Propagation, Phase 1, AFATL-TR-71-95, August 1971.

40. Sih, G. C., G. T. Embley, and R. S. Ravera, "Impact Response of a Finite Crack in Plane Extension", Int. J. Solids and Structures, 8, 977-993, 1972.

41. ASTM Committee E-28 on Mechanical Testing, "Standard Methods for Notched Bar Impact Testing of Metallic Materials", ASTM Standard E23-66, American Society for Testing and Materials, 1971.

42. Turner, C. E., "Measurement of Fracture Toughness by Instrumented Impact Test", Impact Testing of Metals, ASTM STP 466, American Society for Testing and Materials, 466, 93-114, 1970.

43. Venzi, S., A. H. Priest, and M. J. May, "Influence of Inertial Load on Instrumented Impact Tests", Impact Testing of Metals, ASTM STP 466, American Society for Testing and Materials, 1970, 165-180.

44. Davis, P. J., and P. Rabinowitz, Numerical Integration, Blaisdell, 1967.

45. Filon, L. N. G., "On a Quadrature Formula for Trigonometric Integrals", Proc. Roy. Soc. Edinburg, 49, 38-41, 1929.

46. Chase, S. M., and L. D. Fosdick, "An Algorithm for Filon Quadrature", Comm. of the ACM, Vol. 12, No. 8, 453-457, 1969.

47. Chase, S. M., and L. D. Fosdick, "Algorithm 353, Filon Quadrature (D1)", Comm. of the ACM, Vol. 12, No. 8, 457-458, 1969.

48. Hildebrand, F. B., Introduction to Numerical Analysis, McGraw-Hill, 1956.

49. Abramowitz, M., and I. A. Stegun, Handbook of Mathematical Functions, Dover, 1965.

50. King, W. W., J. M. Anderson, and J. D. Morgan, "Dynamics of Cracked Structures Using Finite Elements". Presented to the 13th Annual Symposium on Fracture and Flaws, Albuquerque, New Mexico, March 1973.

51. Radon, J. C., and C. E. Turner, "Fracture Toughness Measurements by Instrumented Impact Test", Engineering Fracture Mechanics, 1, 411-428, 1969.

52. Symposium on Fracture Toughness Testing and Its Applications, ASTM STP 381, American Society for Testing and Materials, 1964.

53. Brown, W. F., and J. F. Srawley, Plane Strain Crack Toughness

Testing of High Strength Metallic Materials, ASTM STP 410, American Society for Testing and Materials, 1966.

54. Isida, M., Crack Tip Stress Intensity Factors for the Tension of an Eccentrically Cracked Strip, Lehigh University, Department of Mechanics Report, 1965.

55. Muskhelishvili, N. I., Some Basic Problems of the Mathematical Theory of Elasticity, Noordhoff, 1963.

56. Nash, G. E., "An Analysis of the Forces and Bending Moments Generated During the Notched Beam Impact Test", Int. J. Fracture Mechanics, 5, 269-286, 1969.

57. Server, W. L., and A. S. Tetleman, "The Use of Pre-Cracked Charpy Specimens to Determine Dynamic Fracture Toughness", Engineering Fracture Mechanics, 4, 367-375, 1972.

58. Langhaar, H. L., Energy Methods in Applied Mechanics, Wiley, 1962.

59. Lanczos, Cornelius, The Variational Principles of Mechanics, 3rd Edition, University of Toronto Press, 1966.

60. Dunham, R. S., R. E. Nickell, and D. C. Stickler, "Integral Operators for Transient Structural Response", Computers and Structures, 2, 1-15, 1972.

61. Wilson, E. L., A Computer Program for the Dynamic Stress Analysis of Underground Structures, Report Number 68-1, University of California at Berkeley, 1968.

62. Gurtin, M. E., "Variational Principles for Linear Elastodynamics", Archives for Rational Mechanics and Analysis, 16, 34-50, 1964.

63. Becker, E. B., and R. E. Nickell, "Stress Wave Propagation Using the Extended Ritz Method", Proceedings 10th ASME/AIAA Structures, Structural Dynamics and Materials Conference, 1969.

64. Nickell, R. E., "On the Stability of Approximation Operators in Problems of Structural Dynamics", Int. J. Solids and Structures, 7, 301-319, 1971.

65. Nickell, R. E., "Direct Integration Methods in Structural Dynamics", Journal of the Engineering Mechanics Division, ASCE, No. EM2, 303-317, 1973.

66. Timoshenko, S. and S. Woinowsky-Krieger, Theory of Plates and Shells, McGraw-Hill, 1959.

VITA

Joseph David Morgan III was born 6 November 1937 in Gainesville, Florida, the son of Joseph D. and Dorothy Goodbred Morgan. He attended elementary and high schools in Florida and Kansas, graduating from P. K. Yonge High School in Gainesville in 1954.

After a year at the University of Florida, he entered the United States Air Force Academy, from which he was graduated with the degree of Bachelor of Science and commissioned a second lieutenant in the United States Air Force in 1959.

After pilot training, he was an instructor pilot at Vance Air Force Base, Oklahoma. In 1966, he entered the Georgia Institute of Technology under Air Force sponsorship and two years later received the degree of Master of Science in Engineering Mechanics. He was a fighter pilot with the 555th Tactical Fighter Squadron in Thailand for a year, and in 1969 was assigned to the Department of Engineering Mechanics at the United States Air Force Academy as an Instructor. In 1971 he returned to the Georgia Institute of Technology under the Air Force Academy's faculty enrichment program.

Major Morgan is married to the former Karen Calhoun. They have four children: Laurie, Leslie, Joseph D. IV and Scott.